FREE-ENERGY BASED MODELING OF PLANAR DIELECTRIC ELASTOMER ACTUATORS

JINGYU FAN

A THESIS

IN

THE DEPARTMENT

OF

MECHANICAL, INDUSTRIAL AND AEROSPACE ENGINEERING

PRESENTED IN PARTIAL FULFILLMENT OF THE REQUIREMENTS

FOR THE DEGREE OF

MASTER OF APPLIED SCIENCE (MECHANICAL ENGINEERING) AT

CONCORDIA UNIVERSITY

MONTRÉAL, QUÉBEC, CANADA

MARCH 2024

CONCORDIA UNIVERSITY

School of Graduate Studies

This is to certify that the thesis prepared

By: **Jingyu Fan**

Entitled: **Free-Energy Based Modeling of Planar Dielectric Elastomer Actuators**

and submitted in partial fulfillment of the requirements for the degree of

Master of Applied Science (Mechanical Engineering)

complies with the regulations of the university and meets the accepted standards with respects to originality and quality.

Signed by the final examining committee:

_____ Chair
Dr. Youmin Zhang

_____ Examiner
Dr. Youmin Zhang

_____ Examiner
Dr. Lan Lin

_____ Thesis Supervisor
Dr. Chun-Yi Su

Approved By _____
Dr. Martin Pugh
Graduate Program Director

_____
Dr. Mourad Debbabi
Dean of the Gina Cody School of Engineering and Computer Science

Abstract

Free-Energy Based Modeling of Planar Dielectric Elastomer Actuators

Jingyu Fan

Dielectric elastomer actuators (DEAs) have gained increasing attention over the last decades and have been widely developed for applications fields such as robots, aerospace, biomedicine due to the fast response, high energy density, light weight, and low cost. However, the task of modeling of DEAs is typically challenged in the presence of the nonlinear features, time-independent viscoelastic behaviors, complex electromechanical coupling, etc.

To address such a challenge, a free-energy based model for DEAs moving in vertical direction is proposed, in an effort to investigate the physical properties of DEAs in this research. The developed model is based on the principle of nonequilibrium thermodynamics, where the Gent model and generalized Maxwell model are applied to describe the free energy and viscoelastic behavior of DEA, respectively. Unlike the existing modeling methods, this research narrows the focus on the inertial force and viscoelasticity which leads to DEA's instability.

After that, the free-energy based model is simulated in MATLAB and the several sets of experiments are implemented by setting various driving voltage amplitudes and frequencies. According to the experimental data, the undetermined parameters of the model are identified by using differential evolutionary algorithm. The comparison of the model simulation and experimental results supports the validation of the proposed free-energy based model.

Acknowledgements

Foremost, I would like to thank my supervisor, Dr. Chun-Yi Su, for his continuous guidance and constant encouragement. Dr. Su's wisdom and patience not only motivated me throughout my study at Concordia University, but also inspired me to be a better researcher and a better person.

I would like to thank Dr. Wenjun Ye and Dr. Yawu Wang who bought great ideas of this topic and supported me with experimental tests.

I am grateful to my colleagues, particularly, Dr. Yue Zhang, Dr. Peng Huang, Dr. Jundong Wu, Dr. Pan Zhang, Dr. Qun Lu, Dr. Yaowei Wang, Dr. Yun Liu, Dr. Nan Xu, and Dr. Ying Zhou for providing a collaborative and pleasant research environment.

Last but not least, heartfelt thanks to my parents, sister for their support.

Contents

LIST OF FIGURES ..... **VII**
LIST OF TABLES ..... **IX**
CHAPTER 1 INTRODUCTION **1**
1.1 MOTIVATION 1
1.2 OBJECTIVE OF THE THESIS 2
1.3 ORGANIZATION OF THE THESIS 3
CHAPTER 2 LITERATURE REVIEW **4**
2.1 SOFT MATERIALS 4
2.2 DIELECTRIC ELASTOMER ACTUATOR 7
2.2.1 DE materials 7
2.2.2 Compliant electrodes 8
2.2.3 Working principle 10
2.2.4 Applications of DE materials 11
2.3 MODELING METHODS 13
2.3.1 General modeling method 14
2.3.2 Free-energy based nonlinear modeling method 17
2.3.3 Elastic material models 20
2.3.4 Viscoelastic material models 23
2.4 SUMMARY 24

CHAPTER 3 FREE-ENERGY BASED MODELING OF PLANAR DIELECTRIC ELASTOMER ACTUATOR 26
3.1 MODEL DESCRIPTION 27
3.2 FREE-ENERGY BASED MODEL 29
3.3 MODEL SUMMARY 34
CHAPTER 4 EXPERIMENTAL PREPARATION AND MODEL VALIDATION 35
4.1 EXPERIMENTAL PREPARATION 35
4.1.1 DEA fabrication 35
4.1.2 Experimental platform 36
4.2 MODEL IDENTIFICATION 37
4.2.1 Driving voltage 38
4.2.2 Parameters identification 38
4.3 MODEL VALIDATION 43
4.3.1 Model validation with different driving voltage amplitudes 43
4.3.2 Model validation with different driving voltage frequencies 48
4.4 SUMMARY 52
CHAPTER 5 CONCLUSION AND FUTURE WORK 53
5.1 CONCLUSION 53
5.2 FUTURE WORK 54
REFERENCES 55

List of Figures

Figure 1 The Deformation Characteristics of DE Actuator and IPMC Actuator... 6

Figure 2 Working Principle of Planar DEA 10

Figure 3 (a) Rheological Model and (b) Maxwell Model 23

Figure 4 (a) Generalized Kevin Model and (b) Kevin-Voigt Model 24

Figure 5 Schematic of The DEA, (a) Initial State, (b) Pre-Stretching State, and (c) Electro-Deformed State 27

Figure 6 The Generalized Maxwell Model 30

Figure 7 Structure of Planar DEA 36

Figure 8 Block Diagram of Experimental Platform 37

Figure 9 Diagram of Driving Voltage Set for Parameters Identification 39

Figure 10 Comparison of Model Simulation and Measured Experimental Data with Different Amplitudes and Frequencies 42

Figure 11 Comparison of Model Simulation and Measured Experimental Data with Driving Voltage Frequency $\boldsymbol{fi = 0.2}$ (Hz) 44

Figure 12 Comparison of Model Simulation and Measured Experimental Data with Driving Voltage Frequency $\boldsymbol{fi = 0.4}$ (Hz) 45

Figure 13 Comparison of Model Simulation and Measured Experimental Data with Driving Voltage Frequency $\boldsymbol{fi = 0.8}$ (Hz) 46

Figure 14 Comparison of Model Simulation and Measured Experimental Data with Driving Voltage Amplitude $\boldsymbol{ai = 6.0}$ (kV) 49

Figure 15 Comparison of Model Simulation and Measured Experimental Data with Driving Voltage Amplitude $\boldsymbol{ai} = \mathbf{7.0}$ (kV).....50
Figure 16 Comparison of Model Simulation and Measured Experimental Data with Driving Voltage Amplitudes $\boldsymbol{ai} = \mathbf{8.0}$ (kV).....51

List of Tables

Table 1 Comparison of Different Types of Smart Materials with Typical Values. 5
Table 2 Comparison of Various Compliant Electrodes. 9
Table 3 Identified Parameters of Free-Energy Based Model. 43
Table 4 Modeling Errors with Different Driving Voltage Amplitudes $\boldsymbol{ai}$. 47
Table 5 Modeling Errors with Different Driving Voltage Frequencies $\boldsymbol{fi}$.....52

Chapter 1

Introduction

1.1 Motivation

Over the last decade, dielectric elastomer (DE) materials characterized by flexible and deformable structures and low stiffness, have garnered significant attention from both the academic and industrial communities. Their unique physical characters present great potential in the application such as electronics, mechanics, biomedicine, aerospace, and thermodynamics, leading the way in the innovation of various fields[1][2]. In comparison to traditional rigid materials, DE materials can be applied to execute diverse tasks in complex and irregular working environments and possess higher adaptability and safety[3]. Hence, DEs are increasingly recognized as alternatives to traditional rigid materials[4]. The dielectric elastomer (DE) material, which is a typical type of electro-active polymer (EAP) materials can convert electrical energy into mechanical energy[5]. Nowadays, DEs are widely utilized as dielectric elastomer actuators (DEAs), dielectric elastomer generators (DEGs), and dielectric elastomer sensors (DESs) due to their properties such as electro-induced stain, rapid response, lightweight, low cost, flexible motion, high energy density, and resistance to fatigue damage.

Meanwhile, DEAs are facing challenges in their complex nonlinear characteristics such as the inherent nonlinearity, time-dependent viscoelastic behaviors, hysteresis, creep, vibrational dynamics, and complicated electromechanical coupling[6]. Therefore, there is a growing effort to investigate and develop the dynamic model of DEAs.

1.2 Objective of the thesis

With the aim of understanding and controlling the performance of DEAs, as well as their feasibility in practical applications, many researchers have devoted their contributions to the mechanism modeling. However, most of the previous research focused on static or quasi-static models to explicate the behaviors of DEA, which also ignored the inertial force and time-dependent viscoelastic behavior[7].

Besides, some scholars use Very High Bond (VHB) to fabricate DEA, which is a polyacrylate material produced by 3M and renowned for its outstanding adhesive strength. Nevertheless, the shortcomings of VHB are obvious, which has high viscoelasticity. As the other common class of DE materials, polydimethylsiloxane (PDMS) stands out as a promising substitute to address the significant viscoelastic challenges, with its potential largely unexplored in current research.

The focus of this thesis is to develop a mechanism model of planar DEAs fabricated by PDMS material. Based on the free-energy method, the proposed model highlights the inertial force and nonlinear time-dependent viscoelastic behavior of DEA. Then, the differential evolutionary algorithm is employed to identify the undetermined model parameters under the experimental platform. Finally, the validity of the proposed model is demonstrated to test the effectiveness by setting various driving voltage amplitudes and frequencies.

1.3 Organization of the thesis

This thesis consists of 5 chapters including the introduction in **Chapter 1**. The remaining part of this thesis is organized as follows.

Chapter 2:

Extensive literature review is presented, which encompasses soft materials, dielectric elastomers (DEs), and various modeling methodologies.

Chapter 3:

A free-energy based model of planar dielectric elastomer actuator (DEA) moving in vertical direction is developed.

Chapter 4:

The experimental setup, simulations, and data collection procedures used in this research are meticulously outlined. Additionally, it elucidates the validation process of the proposed model, engaging in both theoretical and experimental comparisons. Furthermore, the accuracy of the model is thoroughly addressed.

Chapter 5:

Summary of this research is presented and followed by concluding remarks.

Chapter 2

Literature Review

2.1 Soft materials

The actuation of soft materials hinges predominantly on their distinctive properties and exhibit responsive behavior to various stimuli, encompassing electric fields, pressure, magnetic field, a change in pH, light, and temperature, enabling them to achieve versatile and agile movements[8]. Electro-active polymer (EAP), ionic polymer-metal composite (IPMC), liquid crystal elastomer (LCE), shape memory alloy/polymer (SMA/SMP), and others are currently well-known soft materials and widely researched[8]. To have an overview of the performances of different soft materials, the comparison with typical values is listed in Table 1.

Category	**Stimuli**	**Strain** (%)	**Stress** ($\boldsymbol{MPa}$)	**Response speed** ($\boldsymbol{Hz}$)	**Energy conversion efficiency** (%)
SMA	Heat	10	200	< 1	10
SMP	Heat	400	4	< 0.5	10
IPMC	Electricity	~50	~0.5	10	30
DE	Electricity	380	~8	> 100	85

Table 1: Comparison of different types of smart materials with typical values

Among various soft materials, polymer-based smart materials have attracted widespread attention in the academic community due to their advantages such as lightweight, large deformation, good biocompatibility, excellent fatigue life, and low cost. In the category of polymer-based materials, electro-active polymer (EAP) is a novel and highly regarded functional material that has attracted the most significant attention. Under the excitation of external electric field, EAP materials can significantly alter their own shape and size. Once the external excitation is removed, they can return to their original shape and size. In addition, this effect is reversible, meaning that even if EAP materials deform under external forces, they can generate corresponding electric signals as output. Hence, EAP materials are a newly developed style of flexible soft materials with dual functions of sensing and actuation in recent years[9].

According to different actuation mechanisms, EAP materials are mainly divided into ionic polymer-metal composite (IPMC) and dielectric elastomer (DE)[11]. The driving voltage required for IPMC is relatively low, and its actuation principle involves significant deformation caused by the redistribution of ions and solvents within the film in response to an electric field. The

movement of ions requires to be assisted in a solution environment, so IPMC needs to maintain a wet surface while working. Compared to DE materials, IPMC generally exhibits slower response speed[12]. DE has no specific environmental requirements and can deform in the air, but it requires high driving voltage (or electric field strength). The actuation principle of DE involves the generation of electrostatic stress within the film in response to an electric field, causing a significant deformation inducing changes in molecular structure.

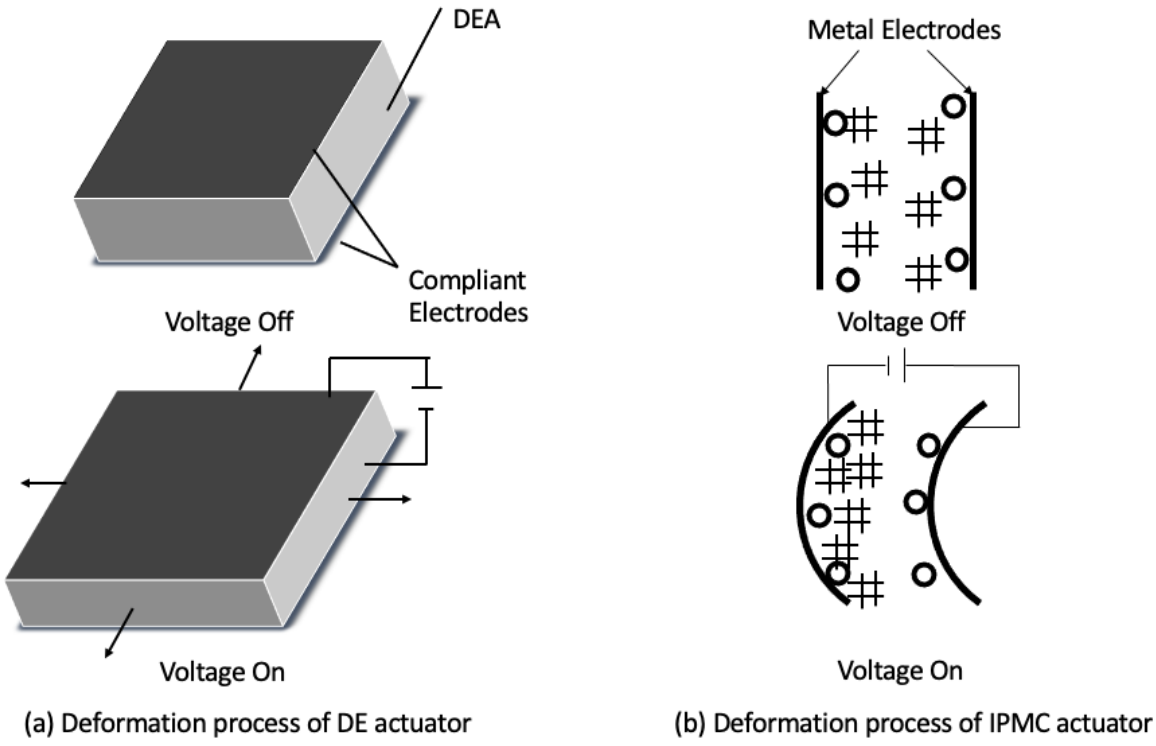

Figure 1: The deformation characteristics of DE actuator and IPMC actuator

Fig. 1 shows the deformation characteristics of DE actuator and IPMC actuator. It can be observed that with the stimuli of an electric field, DE undergoes compressive deformation in the direction consistent with the electric field and internal expansion deformation perpendicular to it. In contrast, IPMC undergoes bending deformation with the stimuli of an applied voltage[13].

Dielectric elastomer actuators (DEAs) possess the advantages of high energy density, large strain, low cost, lightweight, and commercially available, rendering them the subject of extensive study and research[14]. Subsequent sections delve into further details about DEAs.

2.2 Dielectric elastomer actuator

The deformation scale of DE materials is remarkably large, typically reaching up to 380%. They exhibit millisecond-level response speed, with a maximum stress capacity of $3.2MPa$, an energy density of $3.4J/g$, and an impressive mechanical-to-electrical conversion efficiency of up to 80%[15].

2.2.1 DE materials

According to the working principle of DEAs, any insulating polymer film can have deformation under the stimuli of an electrical field, with the physical properties of the film determining the scale of its deformation. In the past research, the results can be obtained that the deformation is small when the elastic modulus of DEAs is high[16][17]. And with the increase of voltage, the material would experience electrical breakdown before significant deformation occurs[18]. Therefore, with the purpose of being used as large deformation actuators, DE materials should possess low elastic modulus, low viscosity, high electrical breakdown strength, and high dielectric constant to achieve large-scale strain output. Researchers have discussed various DE materials, and the most frequently used materials are acrylics, silicones, and polyurethanes (PUs)[17].

Because acrylic polymers (VHB 4910 and VHB 4905, fabricated by 3M company) are readily available and inexpensive, they are the primary materials in the current research and application

fields of DEAs. From the prospective of performance, 3M VHB exhibits a larger area stain and a relatively high dielectric constant compared to other DE materials[19]. However, the disadvantage of 3M VHB is its high viscoelasticity which affects the stability of deformation[20]. To solve this problem, polydimethylsiloxane (PDMS) as the other class of DE materials has attracted researchers' attention. In this study, we will investigate the mechanism modeling of DEA based on PDMS.

2.2.2 Compliant electrodes

Due to the flexible nature of DE materials, ideal electrodes should possess excellent conductivity and low resistance under large strain. Currently, commonly used compliant electrode materials include carbon grease, graphite powders, graphite spray, and thickened electrolyte [21]. Table 2 provides a comparison of various options that can be used as compliant electrodes for DEAs. In practical use, carbon grease has the best adhesion characteristic, stable performance, and good conductivity, making it the most widely used electrode material[22]. The processing technology for other electrode materials is more intricated, with higher requirements and higher costs, resulting in limited applications.

Electrode	Resistivity	Application	Advantages	Disadvantages
Carbon grease	$50k\Omega/cm$	Thin film deposition	High electromechanical coupling efficiency	Uneven surface
Graphite powders	$80k\Omega/cm$	Screen printing	Stable performance	Non-adhesive
Graphite spray	$20k\Omega/cm$	Spray	Uniform surface	Non-adhesive
Thickened electrolyte	$15k\Omega/cm$	Thin film deposition	Good performance at low voltages	Easy to evaporate
Silver paste	$1.6\mu\Omega/cm$	Thin film deposition	Good conductivity	Easy to evaporate
Conductive polymer	$51\mu\Omega/cm$	-	Good compliance and elastic properties	Poor performance and stability

Table 2: Comparison of various compliant electrodes

2.2.3 Working principle

As shown in Fig. 2, the structure of DEAs is sandwiched with a core layer of polymer film and compliant electrodes on both sides. The polymer film undergoes expansion in area and compression in thickness under the stimuli of an electric field, which can be perfectly explained by Maxwell's stress theory[23]. The compliant electrodes transmit external voltage signals to the surface of DE film, serving as conductive function. Because the conversion between electrical energy and mechanical energy is reversible, DEs can be used as energy harvesters[24]. Clearly, the selections of DE material and compliant electrodes have an impact on the performance of DEAs.

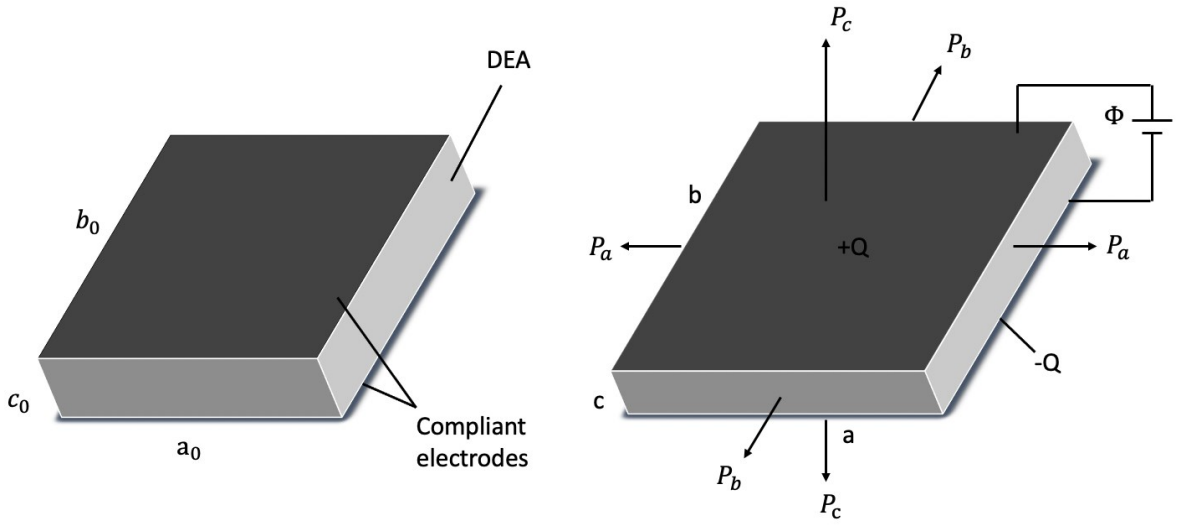

Figure 2: Working principle of planar DEA

The initial dimension before deformation is $a_0 \times b_0 \times c_0$. When the voltage Φ and mechanical forces in three directions P_a, P_b, P_c are applied, the upper and bottom surfaces of DEA accumulate positive and negative charges $\pm Q$ due to polarization. The electrostatic Coulomb forces generated by the attraction of these opposite charges cause DEA to decrease in thickness and expand in the plane area. Under the simultaneous action of external force and voltage load, the dimensions of

the structure after deformation are represented as $a \times b \times c$. Besides, the strain of each dimension can be expressed by $\lambda_a = \frac{a}{a_0}$, $\lambda_b = \frac{b}{b_0}$, and $\lambda_c = \frac{c}{c_0}$, respectively. And DEAs are assumed as incompressible, which means the volume of the film maintain constant. Hence, we can obtain $\lambda_a \lambda_b \lambda_c = 1$.

2.2.4 Applications of DEAs

Through a decade of sustained research on DE materials, their widespread applications have extended across diverse fields, such as healthcare, rescue operations, and human-robot collaboration[25]. Based on diverse configurations of DEAs, these applications aim to achieve complex tasks in uncertain environments. In the following section, some interesting applications are introduced.

Swimming robots

Deep-sea robots, as a crucial technology in current marine exploration, play a pivotal role in the fields of undersea exploration and rescue operations[26]. Positioned at the forefront of underwater equipment, soft swimming robots take soft bodied organisms as bionic prototypes, utilizing highly flexible and elastic materials. In terms of function, they are actuated or sensed by intelligent soft materials instead of traditional motors or sensors, hereby overcoming the challenges posed by extreme water pressure. Because of their unique strong adaption, high flexibility, self-awareness and other advantages, soft swimming robots have shown immense potential in the deep-sea field applications[27].

A swimming robot featuring flapping fins fabricated by DEA was developed[28]. And it successfully descended the seabed of Mariana Trench, achieving a stable fluttering motion at a remarkable depth of $10,900$ meters. Additionally, through careful design, it achieved autonomous swimming at $3{,}224$ meters in the South China Sea. A jellyfish robot powered by a DEA was designed[29], which can navigate efficiently in water. It has the capability to expel water for propulsion. Moreover, the muscle-like actuator functions as a deformable bladder, enabling the adjustment of the buoyant force acting on the soft robot[30].

Wall-climbing robot

Wall-climbing robots represent an important advancement in mobile robotics by integrating traditional mobility with adsorption technology, thereby substantially broadening the spectrum of applications for robotics[31]. With scientists' forward-thinking imagination and rapid abilities to learn from nature, the soft wall-climbing robots actuated by DEs were established, achieving stable wall-climbing, horizontal crawling, and in-situ turning through synergistical control mechanism that regulates the deformation of the DEA and the magnitude of the electrostatic adsorption force.

The soft wall-climbing robot jointly developed by Shanghai Jiao Tong University and MIT is notable for its compact design, weighing only $2g$ and measuring $85mm$ in length[32]. Its distinctive feature is the ability to complete wall climbing tasks while carrying certain heavy objects. This innovation demonstrates promising applications in detection, search, and rescue operations within vertical narrow spaces, as well as effective wall cleaning.

Soft tunable lenses

Inspired by certain insects and human eyes, the development of soft tunable lenses has ushered in a new era for cameras, smartphones, and other optical devices. Unlike the traditional focus lens, tunable lenses can dynamically change the focal length driven by responsive materials[33]. In addition, they can fully leverage the compact characteristics of intelligent materials to reduce the weight of devices.

The soft focus-tunable lenses were designed which consist of a zipping-shaped DEA to achieve the ability of tuning the focal length[34]. Under a driving voltage signal below $500V$, the focal length can be rapidly changed between 550 and $22mm$ within milliseconds. Another research group successfully created a soft lens using a disk-type DEA pair[35]. And at the annular center of the DEA configuration, the soft lens with a $3mm$ diameter undergo efficient stretching, resulting a remarkable change of 65.7% in focal length when applied a voltage.

2.3 Modeling methods

To better study the deformation mechanism of DEAs, it's necessary to develop a reasonable and effective model. More and more scholars have established the dynamic models that are characterized by strong theoretical foundation, comprehensive descriptions of DEAs, and good applicability. In the early research, some static and quasi-static models were developed to explain the deformation of DEAs. For example, the quasi-static force-displacement relationship of a conical DEA was described by Cao[36]. And a quasi-static model was developed to characterize the performance of a double cone DEA[37]. From the modeling processes in previous research, it's obvious that the inertial force was ignored, and the viscoelastic behavior wasn't taken into

consideration. A dynamic model based on an equivalent slider-crank mechanism was presented[38], where the Lagrange equation was employed to describe both geometric and viscoelastic nonlinearities. Huang et al.[39] proposed a dynamic model of DEAs with a conical shape to describe the stress-strain relationship on the basis of nonequilibrium thermodynamics which is introduced in detail in the following section.

Generally, the modeling methods of DEAs can be divided into two classes including general electromechanical modeling method and free-energy based modeling method. In the following sections, the details of these modeling methods are introduced.

2.3.1 General modeling method

Initially, the academic community believed that Maxwell stress was the primary factor causing deformation in DEAs[40]. Maxwell stress p is described by an applied voltage Φ and film thickness d as

$$p = \varepsilon \left(\frac{\Phi}{d}\right)^2 \tag{1}$$

where ε denotes the DEA's permittivity. The results of Eq. (1) align well with experimental observations of electrostatically induced deformation stress in DEAs under direct current voltage. As research progressed, researchers found that, under the stimuli of electric field, the electrostatic forces in highly deformable DEAs should originate from two aspects: Maxwell stress and electrostriction stress. Both stresses are proportional to the square of the electric field. Comparatively, Maxwell stress is the main factor, constituting a significant proportion of the electrostatic stress. The accumulation of opposite charges on the surfaces of the DEAs on both

sides results in electrostatic Coulomb forces attracting each other. The electrostatic forces compress the materials in the thickness direction, causing a decrease and expansion in the plane direction of DEAs. This deformation is independent of the variation in the DEA's permittivity. On the other hand, the generation of electrostriction stress is associated with changes in the DEA's permittivity.

DEAs' ability of generating mechanical force by electrical field is referred to as electromechanical coupling. Pelrine et al. developed a physical model which explains the electromechanical coupling of DEAs in 1998[41]. The effective stress p_{el} is described by an applied voltage Φ and film thickness d as

$$p_{el} = \varepsilon_0 \varepsilon_r \left(\frac{\Phi}{d}\right)^2 = \varepsilon_0 \varepsilon_r E^2 \tag{2}$$

where ε_0 and ε_r denote the free-space permittivity ($8.85 \times 10^{-12}\ Fm^{-1}$) and relative dielectric constant respectively, and E is the electric field. Then Pelrine and his colleagues presented a straightforward approach for predicting DEA strains by applying Hooke's laws to Eq. (2).

$$s_{el} = -\frac{p_{el}}{Y} = -\varepsilon_0 \varepsilon_r \frac{E^2}{Y} \tag{3}$$

where s_{el} denotes the thickness strain and Y is the elastic modulus associated with the strain.

However, based on detailed analysis, the instability exists at -33% thickness strain with free boundary conditions which could cause the collapse in thickness. For this reason, based on the structure of a parallel-plate capacitor, Wissler employed an electromechanical model of DEAs with large deformation [42]. When a voltage U is applied to a parallel-plate capacitor with the capacitance C, the stored electrostatic energy W_{el} is given by

$$W_{el} = \frac{1}{2} C U^2 \tag{4}$$

When the capacitor undergoes deformation, the electrostatic energy W_{el} is converted to mechanical energy W_m. At this point, for a thin film capacitor with an overall thickness Z,the change in energy per unit thickness z of the material is equal to the force P generated by the voltage. Therefore, we have

$$P = \frac{dW_m}{dz} = \frac{dW_{el}}{dz} \tag{5}$$

Dividing this force by the area A of the capacitor, we obtain the stress as

$$p_z = \frac{dW_m}{dz}\frac{1}{A} = \varepsilon_0 \varepsilon_r \left(\frac{U}{Z}\right)^2 \tag{6}$$

where ε_0 and ε_r denote the free-space permittivity ($8.85 \times 10^{-12}\ Fm^{-1}$) and relative dielectric constant respectively. And Eq. (6) is the expression for Maxwell stress.

Due to the physical properties of DEAs, the internal stress after deformation is composed of multiple sources[41]. The stress in DEAs can be expressed as

$$\sigma = \sigma_E + \sigma_M \tag{7}$$

where σ_E and σ_M denote elastic stress and Maxwell stress, respectively.

In the modeling, it's assumed that the DEAs is a hyperplastic material, meaning the stress-strain relationship doesn't follow the traditional Hooke's law. However, the deformation can recover to its initial state once the load is removed. Additionally, it's assumed to be homogeneous. The

expression can be represented through the deformation gradient tensor, and the total effective stress is given by

$$\sigma = \frac{\rho_m}{\rho_0}\frac{\partial \Sigma}{\partial F}\boldsymbol{F} + p_M \boldsymbol{I} + \sigma_M \tag{8}$$

where ρ_m and ρ_0 denote the density after deformation and density before deformation. When the DEA is considered incompressible, $\rho_m = \rho_0$ and there exists constraint stress p_M; when the DEA is considered compressible, $\rho_m \neq \rho_0$ and there doesn't exist p_M. $\boldsymbol{F}$ is the deformation gradient tensor, $\boldsymbol{I}$ is the unit tensor, and Σ is the internal energy of DEAs per unit volume.

2.3.2 Free-energy based nonlinear modeling method

In 2008, Suo utilizing the classic thermodynamics and the theory of Helmholtz free energy, derived a system of equations by analyzing the transformation between electrostatic energy and elastic strain energy in DEAs during the electromechanical coupling process[43].

Based on the framework of classic equilibrium thermodynamics, Suo assumed that the temperature remains the same before and after deformation of DEAs, and there is no heat exchange with the surroundings[43]. Moreover, only the elastic deformation of DEAs is considered, and the influence of viscoelasticity is neglected.

In Fig. 2, mechanical forces in three directions and the applied voltage together constitute a thermodynamic system. The change of DEAs' Helmholtz free energy is denoted as $\delta\Psi$, the work done by mechanical forces in three directions during the deformation process is denoted as $P_a\delta a + P_b\delta b + P_c\delta c$, and the work done by applied voltage is denoted as $\Phi\delta Q$. When DEAs are in the state of equilibrium with external mechanical forces and applied voltage, the change in free energy

is equal to the sum of the work done by the mechanical forces and by the applied voltage, yields to

$$\delta\Psi = P_a\delta a + P_b\delta b + P_c\delta c + \Phi\delta Q \tag{9}$$

where δa, δb, and δc represent the change in three directions of DEAs as shown in Fig. 2.

Therefore, the density of the Helmholtz free energy W is defined as

$$W = \frac{\Psi}{a_0 b_0 c_0} \tag{10}$$

The stretches in three directions λ_a, λ_b, and λ_c are

$$\begin{cases} \lambda_a = \dfrac{a}{a_0} \\ \lambda_b = \dfrac{b}{b_0} \\ \lambda_c = \dfrac{c}{c_0} \end{cases} \tag{11}$$

The true stresses in three directions σ_a, σ_b, and σ_c are

$$\begin{cases} \sigma_a = \dfrac{P_a}{bc} \\ \sigma_b = \dfrac{P_b}{ac} \\ \sigma_c = \dfrac{P_c}{ab} \end{cases} \tag{12}$$

The true electric field E is

$$E = \frac{\Phi}{c} \tag{13}$$

The true electric displacement D is

$$D = \frac{Q}{ab} \tag{14}$$

By combining Eqs. (12), (13), and (14), the change of charges δQ can be obtained as

$$\delta Q = \mathrm{Db\delta a} + \mathrm{Da\delta b} + \mathrm{ab\delta D} \tag{15}$$

Due to the significant deformation of DEAs and the relatively small volume change, it can be ideally considered as incompressible. Hence, we can obtain

$$\lambda_a \lambda_b \lambda_c = 1 \tag{16}$$

From the Eq. (15), it's indicated that the three variables in the electromechanical coupling of DEAs are not independent completely. So, λ_c can be expressed by λ_a and λ_b as

$$\lambda_c = \frac{1}{\lambda_a \lambda_b} \tag{17}$$

Then, the DEAs' density of free energy W can be expressed in terms of three independent variables, yields to

$$W = W(\lambda_a, \lambda_b, D) \tag{18}$$

Ideally, the relationship between the actual electric field and actual electric displacement is

$$E = \frac{D}{\varepsilon} \tag{19}$$

where ε denotes the permittivity constant of the DEAs and $\varepsilon = \varepsilon_0 \varepsilon_r$.

By dividing Eq. (9) by the volume of DEAs $a_0 b_0 c_0$ and combining Eq. (15), we can obtain

$$\delta W = \frac{\sigma_a - \sigma_b + DE}{\lambda_a}\delta\lambda_a + \frac{\sigma_b - \sigma_c + DE}{\lambda_b}\delta\lambda_b + E\delta D \tag{20}$$

The density of free energy W can be represented by the elastic strain energy $W_s(\lambda_a, \lambda_b)$ which relates to the stretch of DEAs and Helmholtz free energy density $\frac{D^2}{2\varepsilon}$ associated with electric polarization as

$$W(\lambda_a, \lambda_b, D) = W_s(\lambda_a, \lambda_b) + \frac{D^2}{2\varepsilon} \tag{21}$$

In the end, for the ideally incompressible DEAs, the condition of equilibrium is equivalent to

$$\sigma_a - \sigma_c = \lambda_a \frac{\partial W_s(\lambda_a, \lambda_b)}{\partial \lambda_a} - \varepsilon E^2 \tag{22}$$

$$\sigma_b - \sigma_c = \lambda_b \frac{\partial W_s(\lambda_a, \lambda_b)}{\partial \lambda_b} - \varepsilon E^2 \tag{23}$$

From the Eqs. (22) and (23), it's observed that the elastic strain energy $W_s(\lambda_a, \lambda_b)$ directly influences the development of the model [44]. Some widely used elastic material models are introduced in the following part.

2.3.3 Elastic material models

For rubber-like materials which undergo large deformation, the stress-strain state during deformation is often characterized by strain energy functions from the theory of hyperelasticity. Currently, elastic models representing the strain energy functions $W_s(\lambda_a, \lambda_b)$ of DEAs can be

divided into two overall classes: based on Gaussian distribution and based on non-Gaussian distribution hyperelastic strain energy models. Elastic models based on Gaussian distribution mainly include Neo-Hookean model, Yeoh model, Mooney-Rivlin model, and Ogden model[45]. What these elastic models have in common is the assumption that the responsive strain of hyperelastic materials is far from reaching the tensile strength limit of the materials during deformation[46]. And Neo-Hookean model serves as a typical representative in this regard. However, elastic models based on non-Gaussian distribution believe that the deformation range of hyperelastic materials is large and any potentially approach the maximum tensile limit of the materials, for example, Arruda-Boyce model[46].

Neo-Hookean model

For incompressible hyperelastic materials, the Neo-Hookean model has the advantages of the minimum number of parameters and the simplest form[47]. However, from the perspective of experimental results, the relation between stress and strain could transfer linear to nonlinear when reaching a certain point. And the free energy density of Neo-Hookean model is given by

$$W_{Neo}(\lambda_a, \lambda_b) = \frac{1}{2}\mu\left({\lambda_a}^2 + {\lambda_b}^2 + {\lambda_a}^{-2}{\lambda_b}^{-2} - 3\right) \tag{24}$$

where μ represents the strain shear modulus of the hyperelastic material and it's constant; λ_a and λ_b denote the stretches in directions of the length and width, respectively.

Arruda-Boyce model

The advantage of Arruda-Boyce model lies in the introduction of molecular chain breakage parameters, enabling that it can perform statistical modeling of three-dimensional molecular chains on a microscopic scale[48]. And it can be expressed as

$$W_{A-B}(\lambda_a, \lambda_b) = \mu\sqrt{n}\left[\beta\lambda_{chain} - \sqrt{n}\ln\left(\frac{\sin h\beta}{\beta}\right)\right] \tag{25}$$

where n represents the number of blocks in a single molecular chain, $\lambda_{chain} = \frac{1}{3}({\lambda_a}^2 + {\lambda_b}^2 + {\lambda_a}^{-2}{\lambda_a}^{-2})$, $\beta = L^{-1}\left(\frac{\lambda_{chain}}{\sqrt{n}}\right)$, and L is the Langevin function.

Gent model

Combining the elastic models based on Gaussian and non-Gaussian distribution, Gent[49] developed a model to describe the nonlinear constitutive properties of impressible hyperelastic materials in a simple mathematical form. Compared to other elastic models, Gent model has the physical description for materials[50]. And the Gent model of impressible hyperelastic materials can be expressed as

$$W_{Gent}(\lambda_a, \lambda_b) = -\frac{1}{2}\mu J_m \ln\left(1 - \frac{{\lambda_a}^2 + {\lambda_b}^2 + {\lambda_a}^{-2}{\lambda_b}^{-2} - 3}{J_m}\right) \tag{26}$$

where μ refers to the strain shear modulus and J_m refers to the limiting stretch. When the parameter J_m approaches infinity, the Gent model is equivalent to the Neo-Hookean model, and when the parameter J_m is not close to infinity, Gent model can describe a more complex constitutive model curve in the tensile state than Neo-Hookean model.

2.3.4 Viscoelastic material models

In earlier research on DEAs, most scholars simplified DEAs' deformation to ideal elastic behavior, assuming that their deformation process is independent of the time[16]. With the deepening research on DEAs, Pelrine[41] was the prominent researcher to find in experiments that although pre-stretched DEAs could generate deformations greater than 100%, the deformation had a significant dependence on the rate of applied load according to the viscoelastic nature of the material. From plenty of previous experimental results, creep, hysteresis, and some other behaviors exist which leads that viscoelasticity cannot be neglect when modeling DEAs. The common viscoelastic models are made up of various connections of Hookean springs to represent elastic component and Newtonian dashpot to characterize the viscosity[51][52].

Rheological model

The rheological model illustrated in Fig. 3(a), also known as generalized Maxwell model, is one of the most popular viscoelastic models which is of great use to describe many primary properties of DEAs[53]. Maxwell model as shown in Fig. 3(b) is composed of a spring E and a dashpot η arranged in series to represent elastic and viscous elements respectively. Based on Maxwell model, rheological model includes an additional parallel spring E_0, and as many Maxwell models are connected in parallel which can effectively describe multiple relaxation times exhibited by DEAs.

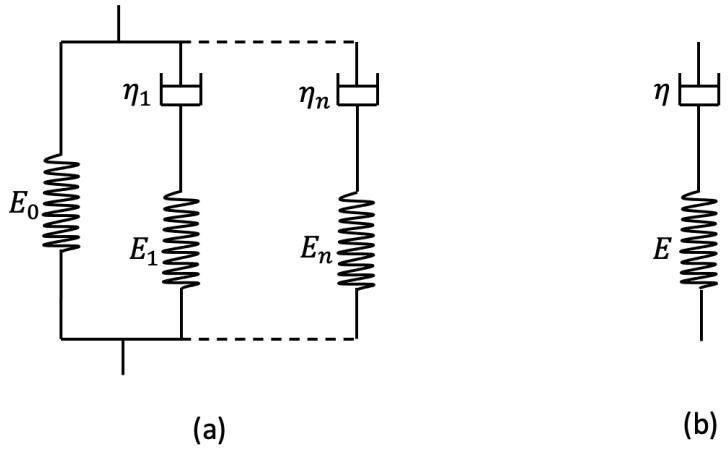

Figure 3: (a) Rheological model and (b) Maxwell model

Generalized Kevin model

The generalized Kevin model as shown in Fig. 4(a), provides a more complex approach to capture multiple relaxation time and is an extension format of Kevin-Voigt model which comprises a spring E and dashpot η in parallel as a pair. Based on the Kevin-Voigt model, an additional spring is included and as many Kevin-Voigt models are connected in series[54].

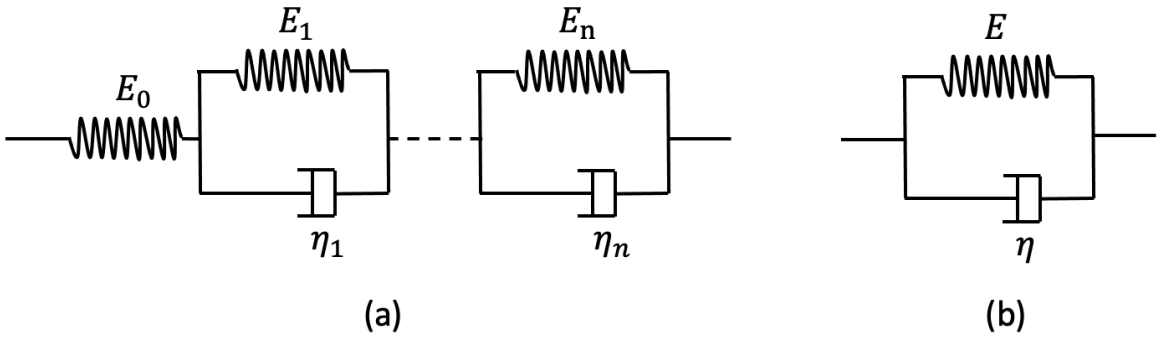

Figure 4: (a) Generalized Kevin model and (b) Kevin-Voigt model

2.2 Summary

The literature review in this research reveals a comprehensive exploration of dielectric elastomer actuators (DEAs) including the working principle, wide applications in different fields, and the various compliant electrodes. Several mathematical models investigated by researchers are introduced, and the comparison between these models sets the foundation for the model selection in further research. In addition, the viscoelastic nature of DEAs is highlighted in this chapter, thus leading to viscoelastic material models which can accurately capture such a behavior.

Chapter 3

Free-Energy Based Modeling of Planar Dielectric Elastomer Actuator

As we learned from previous research, more and more dielectric elastomer actuators have been observed over the last decades. The selection of DEA's configuration must also be considered, as it can significantly impact the strain rate and actuation performance. As it is introduced[17], the planar configuration has more chance to perform high strain rate.

Therefore, in this chapter, a free-energy based model of planar DEA moving in vertical direction is developed to present its electromechanical response and describe its intricate nonlinear viscoelastic behavior. In addition, the Gent model is selected to explain the elastic energy and rheological model is employed to describe its viscoelasticity.

3.1 Model description

Fig. 5 shows the schematic of a planar DEA moving in vertical direction and includes three states. The diagrams of the initial state, pre-stretched state and electro-deformed stated are illustrated in Fig. 5(a), Fig. 5(b), and Fig. 5(c), respectively.

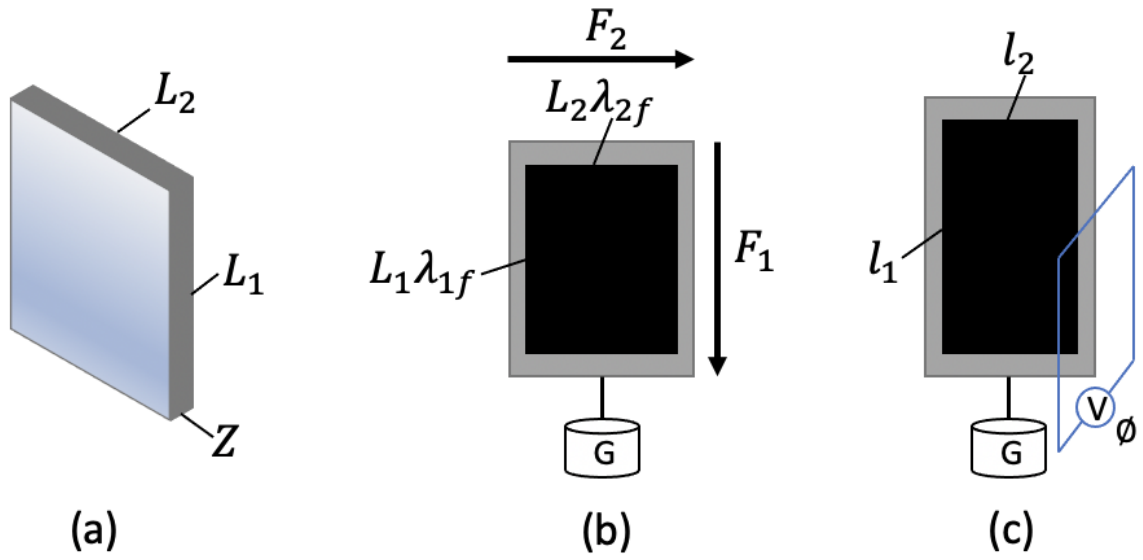

Figure 5: Schematic of the DEA, (a) Initial state, (b) Pre-stretching state, and (c) Electro-deformed state

In initial state, as shown in Fig. 5(a), L_1, L_2, and Z denote the length, width, and thickness of the planar DEA, respectively. In pre-stretching state, there places an object whose gravity is G beneath the DEA with the purpose of better performing the DEA's deformation. At the meantime, in Fig. 5(b), λ_{1f} and λ_{2f} express the length and width stretches of DEA, respectively. Then, the length and width of DEA in pre-stretching state can be expressed as $L_1\lambda_{1f}$ and $L_2\lambda_{2f}$. Once the input voltage $\emptyset$ is applied to the DEA, it comes to the electro-deformed state. As shown in Fig. 5(c), the electric force leads to the mechanical deformation. Hence, the length, width, and thickness of DEA

in this state can be denoted as l_1, l_2 and, z, respectively. And the stretches in three dimensions of DEA can be expressed as

$$\begin{cases} \lambda_1 = \dfrac{l_1}{L_1} \\ \lambda_2 = \dfrac{l_2}{L_2} \\ \lambda_3 = \dfrac{z}{Z} \end{cases} \tag{27}$$

Under the assumption that the DEA is incompressible, then $\lambda_1\lambda_2\lambda_3 = 1$. The true stresses in the length and width dimensions σ_1, σ_2 are denoted as

$$\begin{cases} \sigma_1 = \dfrac{F_1}{l_2 z} \\ \sigma_2 = \dfrac{F_2}{l_1 z} \end{cases} \tag{28}$$

where F_1 and F_2 represent the stresses in the directions of length and width, respectively.

When there is an applied voltage $\emptyset$ in the thickness direction, the relationship between the charge Q on the electrode and the voltage $\emptyset$ is

$$Q = \frac{\varepsilon \emptyset L_1 L_2 (\lambda_1\lambda_2)^2}{z} \tag{29}$$

where ε is the permittivity of the DEA.

The true electric field E is expressed as

$$E = \frac{\emptyset}{z} \tag{30}$$

And the electric displacement D is defined as

$$D = \frac{Q}{l_1 l_2} \tag{31}$$

The free energy of the DEA system is expressed as R. And the total work done by mechanical force in length and width directions can be expressed as $F_1\delta l_1 + F_2\delta l_2$, where δl_1 and δl_2 denote the changes in the directions of DEA's length and width. In the electro-deformed state, the variable of charge is denoted as δQ and the work done by electric force is defined as $\emptyset\delta Q$.

3.2 Free-energy based model

According to the nonequilibrium thermodynamics theory, the increase of the free energy δR is not supposed to exceed the total work done by electric force, mechanical force and inertial force δH, as expressed

$$\delta R \leq F_1\delta l_1 + F_2\delta l_2 + \emptyset\delta Q + \delta H \tag{32}$$

The Helmholtz free energy density of DEA W is denoted as

$$W = \frac{R}{L_1 L_2 Z} \tag{33}$$

By combining Eqs. (32) and (33), the change of the Helmholtz free energy density δW can be obtained

$$\delta W \leq \frac{\sigma_1}{\lambda_1}\delta\lambda_1 + \frac{\sigma_2}{\lambda_2}\delta\lambda_2 + 2\varepsilon\left(\frac{\emptyset}{Z}\right)^2\left(\lambda_1{\lambda_2}^2\delta\lambda_1 + \lambda_2{\lambda_1}^2\delta\lambda_2\right) + \frac{\delta H}{L_1 L_2 Z} \tag{34}$$

In order to describe the viscoelasticity of DE material, we are supposed to select a mathematical model to characterize it. As it is discussed in the section 2.3.4 of viscoelastic material models, there are few options to choose. In this research, the generalized Maxwell model which is also known as rheological model is selected to describe its nonlinear viscoelastic behavior due to the advantage of common usage, flexibility, and simplicity in mechanism. The generalized Maxwell model is illustrated in Fig. 6 and there includes two parts (Part A and Part B). Part A consists of a single spring α_0 and Part B contains several same units which are connected in parallel. And each unit include a spring α_i and a dashpot η_i connected in series, where $i = 1, 2, 3, 4, \dots, n$. Meanwhile, ξ_{ij} is the expression of the stretches of each dashpot, where $j = 1, 2$ and represent the vertical and horizonal directions, respectively. From the organization of the generalized Maxwell model, we can obtain that stretches of each spring α_i can be expressed as $\lambda_{i1} = \frac{\lambda_1}{\xi_{i1}}$ and $\lambda_{i2} = \frac{\lambda_2}{\xi_{i2}}$.

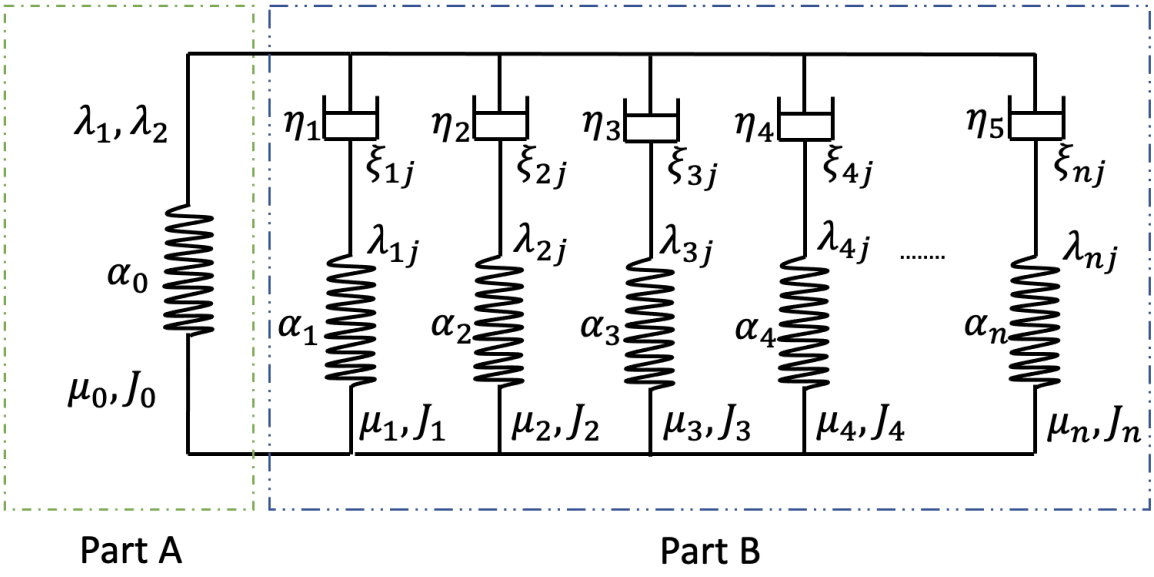

Figure 6: The generalized Maxwell model

From Eq. (21), the free energy density $W(D,\xi_{11},\xi_{12},\xi_{21},\xi_{22},\dots)$ of ideal DEA[43] can be presented as

$$W(D,\xi_{11},\xi_{12},\xi_{21},\xi_{22},\dots)=W_{ela}(\xi_{11},\xi_{12},\xi_{21},\xi_{22},\dots)+\frac{D^2}{2\varepsilon} \tag{35}$$

where $W_{ela}(\xi_{11},\xi_{12},\xi_{21},\xi_{22},\dots)$ is the expression of elastic energy related to stretches of the DEA, ε denotes DEA's permittivity and D is the electric displacement as it is described in Eq. (31).

Here, the Gent model[49] is selected to present the elastic energy density $W_{ela}(\xi_{11},\xi_{12},\xi_{21},\xi_{22},\dots,\xi_{n1},\xi_{n2})$ of the DEA. Based on the organization of the generalized Maxwell model, the free energy density of the DEA can be expressed as

$$\begin{aligned}W_{ela}(\xi_{11},\xi_{12},\xi_{21},\xi_{22},\dots,\xi_{n1},\xi_{n2})=&-\frac{\mu_0 J_0}{2}\ln\left(1-\frac{\lambda_1^2+\lambda_2^2+\lambda_1^{-2}\lambda_2^{-2}-3}{J_0}\right)\\&-\sum_{i=1}^{n}\frac{\mu_i J_i}{2}\ln\left(1-\frac{\lambda_1^2\xi_{i1}^{-2}+\lambda_2^2\xi_{i2}^{-2}+\lambda_1^{-2}\lambda_2^{-2}\xi_{i1}^2\xi_{i2}^2-3}{J_i}\right)\end{aligned} \tag{36}$$

where μ_i denotes shear modulus of the spring α_i and J_i is the deformation limit of the spring α_i respectively.

Since the DEA is incompressible and the volume doesn't change before or after deformation. And there is no pre-stretch in horizonal direction, which means

$$\begin{cases}l_2=L_2\\ \lambda_1=\lambda_{1f}\\ \lambda_2=\lambda_{2f}=1\end{cases} \tag{37}$$

By combining Eq. (37) into (36), we can obtain

$$W_{ela}(\xi_{11},\xi_{12},\xi_{21},\xi_{22},\dots,\xi_{n1},\xi_{n2}) = -\frac{\mu_0 J_0}{2}\ln\left(1-\frac{\lambda_1^2+\lambda_1^{-2}-2}{J_0}\right) - \sum_{i=1}^{n}\frac{\mu_i J_i}{2}\ln\left(1-\frac{\lambda_1^2\xi_{i1}^{-2}+\xi_{i2}^{-2}+\lambda_1^{-2}\xi_{i1}^2\xi_{i2}^2-3}{J_i}\right) \tag{38}$$

Based on the theory of Newton's third law of motion, the true stresses in vertical and horizonal directions σ_1 and σ_2 can be expressed as

$$\begin{cases}\sigma_1 = -\xi_{i1}\dfrac{\partial W_{ela}}{\partial \xi_{i1}} = \eta_i\dfrac{d\xi_{i1}}{dt}\\ \sigma_2 = -\xi_{i2}\dfrac{\partial W_{ela}}{\partial \xi_{i2}} = \eta_i\dfrac{d\xi_{i2}}{dt}\end{cases}(i=1,2,3,\dots,n) \tag{39}$$

From Eqs. (36) and (39), the strain rate of the dashpot in the vertical direction can be obtained as

$$\frac{d\xi_{i1}}{dt} = -\frac{\mu_i}{\eta_i}\frac{-\lambda_1^2\xi_{i1}^{-2}+\lambda_1^{-2}\xi_{i1}^2\xi_{i2}^2}{1-\dfrac{\lambda_1^2\xi_{i1}^{-2}+\xi_{i2}^{-2}+\lambda_1^{-2}\xi_{i1}^2\xi_{i2}^2-3}{J_i}}\ (i=1,2,3,\dots,n) \tag{40}$$

As it is mentioned above, there is no pre-stretch in the horizonal direction. Hence, we can obtain the strain rate of the dashpot in the horizonal direction as

$$\frac{d\xi_{i2}}{dt} = 0\ (i=1,2,3,\dots,n) \tag{41}$$

According to Eqs. (29) and (37), we can get the charge on the electrode varies by

$$\delta Q = \frac{\varepsilon L_1 L_2}{z}(\lambda_1^2\delta\emptyset + 2\emptyset\delta\lambda_1) \tag{42}$$

The work done by inertial forces in each material element along the L_1-direction, L_2-direction and Z-direction are δH_{L_1}, 0, and 0, respectively. Then the total work done by inertial work can be integrated along L_1-direction as follows

$$\delta H_{L_1} = \rho L_2 Z \frac{d^2\lambda_1}{dt^2}\delta\lambda_1 \int_0^{L_1} l^2 dl = -\frac{\rho L_1^3 L_2 Z}{3}\frac{d^2\lambda_1}{dt^2}\delta\lambda_1 \tag{43}$$

The change of the free energy of the DEA is equal to the sum of the works done by the applied voltage, the gravity of the load, and the inertial forces, which means

$$L_1 L_2 D\delta W = \emptyset\delta Q + F_1 L_1 \delta\lambda_1 + \delta H_{L_1} \tag{44}$$

By submitting Eqs. (42) and (43) into (44), we can get the free energy W

$$\delta W = \frac{\emptyset\varepsilon(\lambda_1^2\delta\emptyset + 2\emptyset\delta\lambda_1)}{Z^2} + \frac{F_1\delta\lambda_1}{L_2 Z} - \frac{\rho L_1^2\delta\lambda_1}{3}\frac{d^2\lambda_1}{dt^2} \tag{45}$$

Hence, we can obtain

$$\frac{\partial W}{\partial\lambda_1} = 2\varepsilon\left(\frac{\emptyset}{Z}\right)^2\lambda_1 + \frac{F_1}{L_2 Z} - \frac{\rho L_1^2}{3}\frac{d^2\lambda_1}{dt^2} \tag{46}$$

By submitting Eqs. (31), (35), and (36) into (46), we can get

$$\frac{\rho L_1^2}{3}\frac{d^2\lambda_1}{dt^2} = \frac{F_1}{L_2 Z} + \varepsilon\left(\frac{\emptyset}{Z}\right)^2\lambda_1 - \mu_0\frac{\lambda_1 - \lambda_1^{-3}}{1 - \frac{\lambda_1 - \lambda_1^{-2} - 2}{J_o}} - \sum_{i=1}^{n}\mu_i\frac{\lambda_1\xi_{i1}^{-2} - \lambda_1^{-3}\xi_{i1}^2\xi_{i2}^2}{1 - \frac{\lambda_1^2\xi_{i1}^{-2} + \xi_{i2}^{-2} + \lambda_1^{-2}\xi_{i1}^2\xi_{i2}^2 - 3}{J_i}} \tag{47}$$

3.3 Model summary

Combining Eqs. (40), (41), and (47), the free-energy based model of planar DEA moving in vertical direction can be described as

$$\begin{cases} \dfrac{d\xi_{i1}}{dt} = -\dfrac{\mu_i}{\eta_i}\dfrac{-\lambda_1^2\xi_{i1}^{-2} + \lambda_1^{-2}\xi_{i1}^2\xi_{i2}^2}{1 - \dfrac{\lambda_1^2\xi_{i1}^{-2} + \xi_{i2}^{-2} + \lambda_1^{-2}\xi_{i1}^2\xi_{i2}^2 - 3}{J_i}} \\ \dfrac{d\xi_{i2}}{dt} = 0 \\ \dfrac{\rho L_1^2}{3}\dfrac{d^2\lambda_1}{dt^2} = \dfrac{F_1}{L_2 Z} + \varepsilon\left(\dfrac{\emptyset}{Z}\right)^2\lambda_1 - \mu_0\dfrac{\lambda_1 - \lambda_1^{-3}}{1 - \dfrac{\lambda_1 - \lambda_1^{-2} - 2}{J_o}} \\ \qquad -\displaystyle\sum_{i=1}^{n}\mu_i\dfrac{\lambda_1\xi_{i1}^{-2} - \lambda_1^{-3}\xi_{i1}^2\xi_{i2}^2}{1 - \dfrac{\lambda_1^2\xi_{i1}^{-2} + \xi_{i2}^{-2} + \lambda_1^{-2}\xi_{i1}^2\xi_{i2}^2 - 3}{J_i}} \end{cases} \tag{48}$$

where $i = 1, 2, 3, 4, \ldots, n$.

As stated above, the free-energy based model of planar DEA moving in vertical direction is developed. In the next chapter, the experiment is set up to validate the established model. By employing the differential evolutionary algorithm, the model parameters are identified.

Chapter 4

Experimental Preparation and Model Validation

4.1 Experimental preparation

In this part, the setup process of planar DEA moving in vertical direction and the hardware experimental platform is introduced. Here, polydimethylsiloxane (PDMS) is selected to study and setup the DEA instead of VHB which possesses high viscoelasticity.

4.1.1 DEA setup

As shown in Fig. 7, the planar DEA moving in vertical direction is fabricated. The assembly mainly involves the following four steps:

(1) A DE membrane made of Polydimethylsiloxane (PDMS) with the initial length $L_1 = 0.075m$, initial width $L_2 = 0.072m$, and initial thickness $Z = 0.001m$ as shown in Fig. 5(a), is manufactured by Wacker Chemie AG, Germany.

(2) Compliant electrodes with the material number DD-10 are daubed to the front and back sides of the DE membrane and manufactured by Saidi technology, China.

(3) The load G is measured at the mass $G = 200g$, hence, we can have $\lambda_{1p}L_1 = 0.082m$, and $\lambda_{2p}L_2 = 0.072m$ when at the pre-stretching state as shown in Fig. 5(b).

(4) Frame is made of Polymethyl methacrylate (PMMA).

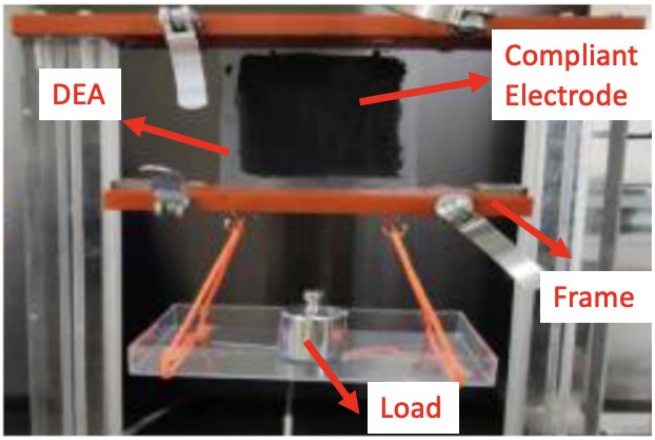

Figure 7: Structure of planar DEA

4.1.2 Experimental platform

The hardware experimental platform (displayed in Fig. 8) is mainly composed of the following five components:

(1) The high voltage amplifier (model number: 10/40A-HS-H-CE) with a gain of 1000, manufactured by TREK, USA, provides the driving voltage for compliant electrodes on the DE membrane.

(2) The laser distance sensor (model number: LK-H152), manufactured by Keyence, Japan, is employed to measure the output displacement of the DE membrane.

(3) The I/O module (model number: PCIe-6361), manufactured by National Instruments, USA, provides the functions of data transfer by generating the control signal for the high voltage amplifier and recording the output signal from the laser sensor.

(4) The computer (CPU: i7-8700, memory: 16G), manufactured by Hewlett Packard, is utilized for date analysis.

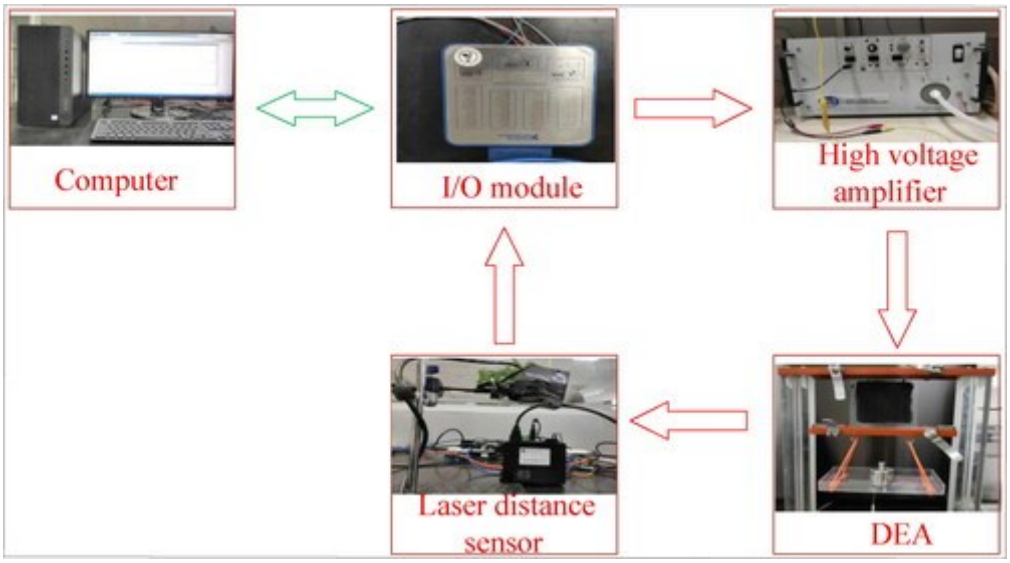

Figure 8: Block diagram of experimental platform

4.2 Model identification

In this section, the developed free-energy based model is characterized by identifying the model parameters and subsequently comparing the model simulation with the experimental results based on the experimental setup. The model parameters are identified through the utilization of differential evolutionary algorithm in MATLAB. Here, taking into account precision and hardware capabilities in the developed model (as shown in Fig. 6), only three spring-dashpot units in parallel connection are considered to characterize the viscoelastic behavior of the DEA.

4.2.1 Driving voltage

The following periodical excitation voltage is applied in order to observe dynamic responses of the DEA.

$$\begin{cases} t_m = rem\left(t, \sum_{i=1}^{5} \frac{1}{f_i}\right) \\ v(t_m) = a_1 \sin(f_1 \pi t_m), \quad 0 \le t_m \le \frac{1}{f_1} \\ v(t_m) = a_2 \sin\left(f_2 \pi t_m - \frac{f_2 \pi}{f_1}\right), \quad \frac{1}{f_1} \le t_m \le \sum_{i=1}^{2} \frac{1}{f_i} \\ v(t_m) = a_3 \sin\left(f_3 \pi t_m - f_3 \pi \sum_{i=1}^{2} \frac{1}{f_i}\right), \sum_{i=1}^{2} \frac{1}{f_i} \le t_m \le \sum_{i=1}^{3} \frac{1}{f_i} \\ v(t_m) = a_4 \sin\left(f_4 \pi t_m - f_4 \pi \sum_{i=1}^{3} \frac{1}{f_i}\right), \sum_{i=1}^{3} \frac{1}{f_i} \le t_m \le \sum_{i=1}^{4} \frac{1}{f_i} \\ v(t_m) = a_5 \sin\left(f_5 \pi t_m - f_5 \pi \sum_{i=1}^{4} \frac{1}{f_i}\right), \sum_{i=1}^{4} \frac{1}{f_i} \le t_m \le \sum_{i=1}^{5} \frac{1}{f_i} \end{cases} \tag{49}$$

where a_i and f_i $(i = 1, 2, 3, 4, 5)$ are the amplitude and frequency, respectively, $t_m = rem\left(t, \sum_{i=1}^{5} \frac{1}{f_i}\right)$ is the remainder of time t and $t \in [0, +\infty)$. When setting various values of a_i and f_i, the driving voltages are generated with different amplitudes and frequencies within one period $T = 0.01\ (s)$.

4.2.2 Parameters identification

From the section 4.1.1 of DEA setup, the experiment parameters L_1, L_2, Z, G, $L_1\lambda_{1f}$, and $L_2\lambda_{2f}$ are given. Here, the value selection of driving voltage amplitudes a_i and frequencies f_i is

introduced first. And DEA's viscoelastic relaxation time $T_i(i = 1, 2, \dots, n)$ is defined as the ratio of η_i to μ_i, then we have

$$T_i = \frac{\eta_i}{\mu_i} \tag{50}$$

Hence, μ_i, J_i, and T_i are the model undetermined parameters and are identified by utilizing differential evolutionary algorithm. Last, to achieve the performance of the model simulation results, the root-mean-square error e_{rms} and the maximum controlling error e_m are discussed.

The amplitude of the driving voltage is set to be $a_i = 5.5 + 0.5i$ (kV) and the frequency of the driving voltage to be $f_i = 0.2i$ (Hz), $(i = 1, 2, 3, 4, 5)$. And the diagram of the driving voltage is displayed in Fig. 9, while the sampling period is set as $T = 0.01$ (s).

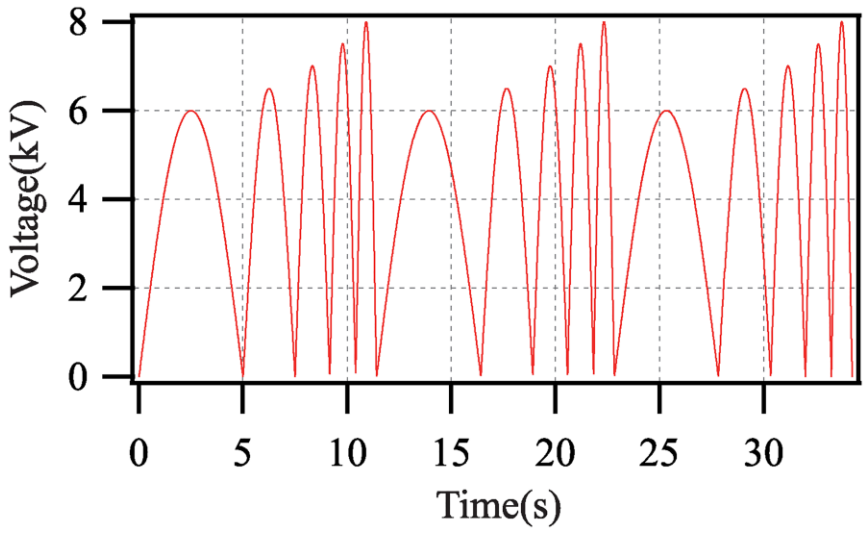

Figure 9: Diagram of driving voltage set for parameters identification

Differential evolution method was first proposed by Storn and Price[55] and has the advantages such as with simple principles, few controlled parameters, and strong robustness. Hence, the differential evolution algorithm is selected to identify and optimise the model parameters in this

research[39][56]. The differential evolutionary algorithm for the identification of the model parameters is briefly listed in Algorithm 1.

Algorithm 1: Differential evolution algorithm

Input: *Voltage signal, DE material and geometrical parameters.*

Output: *Predictions of time-dependent response of DEA*

begin

Input the search ranges of variables of the spring $\boldsymbol{\mu_i}$, $\boldsymbol{J_i}(i = 0, 1, 2, \dots, n)$, *and the relaxation time of the dashpots* $\boldsymbol{T_i} = \frac{\boldsymbol{\eta_i}}{\boldsymbol{\mu_i}}(i = 1, 2, \dots, n)$ *as* K_μ, K_J, *and* K_T, *Then initialize* $g = 0$

Input the dielectric permittivity $\boldsymbol{\varepsilon}$ *of DEA, geometrical parameters* $\boldsymbol{L_1}$, $\boldsymbol{L_2}$, *and* $\boldsymbol{Z}$

Input the voltage signal in Eq. (49)

According to K_μ, K_J, *and* K_T, *randomly initialize the initial population as* $x_k(0)(k = 1,2, \dots, N)$, *where* $x_k = \{\tilde{\mu}_i^k(0), \tilde{J}_i^k(0), \tilde{T}_i^k(0)\}$

For $g = 0{:}\,A$ ***do***

Substituting $x_k(g)$ *into the system model in Eq. (48). Then, call the* ***ode15s*** *function to get* $\tilde{\xi}_{i1}^k(g)$ *and* $\tilde{\xi}_{i2}^k(g)$ *by solving Eq. (48)*

According to the experimental data and $\tilde{\xi}_{i1}^k(g)$ *and* $\tilde{\xi}_{i2}^k(g)$, *calculate Eq. (50)*

> ***If*** $e_{rms} < \delta$ *(*δ *is a small positive constant)****, then***
>
> *The parameters in free-energy based model are obtained. That is,* $\boldsymbol{\mu_i} = \tilde{\mu}_i^k(g)$, $\boldsymbol{J_i} = \tilde{J}_i^k(g)$, *and* $\boldsymbol{T_i} = \tilde{T}_i^k(g)$
>
> ***Break***

End if

According to the mutation rate p_m *and the crossover* p_c, *update* $x_k(g)$ *by executing mutation operation, crossover operation, and selection operation in turn*

End For

Without prior knowledge about the values of model parameters μ_i, J_i and T_i, here we set the search range K_μ of μ_i, K_J of J_i and K_T of T_i as $K_\mu \in (0,\ 8\times10^6)$, $K_J \in (0,\ 9\times10^8)$ and $K_T \in (0,\ 3\times10^6)$, respectively. The maximum number of evolutions A is set as 150. The constant δ is set to be 0.001. The mutation time p_m and crossover rate p_c are set as 0.6 and 0.9, respectively. In addition, the dielectric permittivity ε of DEA is set as $4.7\epsilon_{air}$, where $\epsilon_{air} = 8.85\times10^{-2}$ is the permittivity of vacuum.

The root-mean-square error e_{rms} and the maximum modeling error e_m are discussed as follows to better explain the performance of the model simulation results.

$$\begin{cases} e_{rms} = \sqrt{\dfrac{1}{n}\displaystyle\sum_{i=1}^{n}(z_{ei}-z_{mi})^2}\times100\% \\ e_m = \dfrac{\max(|z_{ei}-z_{mi}|)}{\max(z_{mi})-\min(z_{mi})}\times100\% \end{cases} \tag{50}$$

where z_{ei} and z_{mi} denote the experimental data and the predicted displacement in the vertical direction, respectively; n represents the total amount of data. Besides, the expression $z_{ei}-z_{mi}$ is employed to describe the error between the model simulation and the experimental result.

Based on that we select three spring-dashpot units in generalized Maxwell model for the experiment conduction, the root-mean-square error $e_{rms} = 2.13\%$ and the maximum modeling error $e_m = 4.07\%$. In this way, the comparison of the model simulation and experiment result with different amplitudes and frequencies of driving voltage is shown in Fig. 10. And all the identified parameters of the developed free-energy based model are listed in Table 3.

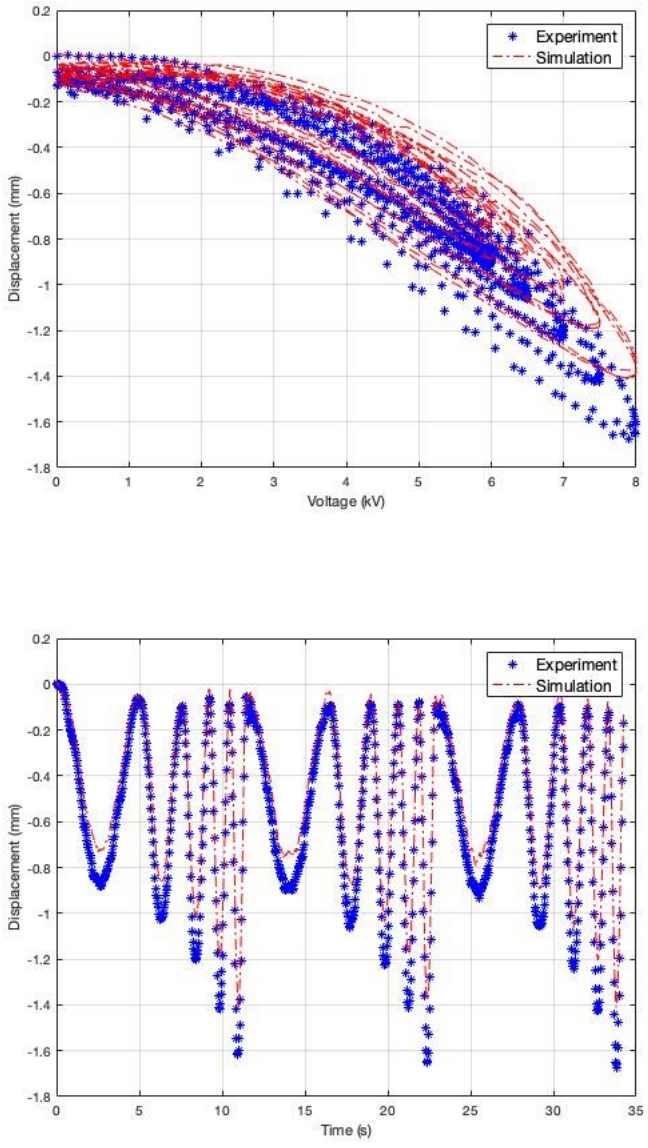

Figure 10: Comparison of model simulation and measured experimental data with different amplitudes and frequencies

	$i = 0$	$i = 1$	$i = 2$	$i = 3$
μ_i	4.5772×10^4	4.0037×10^4	5.1736×10^4	2.3021×10^2
J_i	9.7749×10^3	4.2709×10^3	9.5677×10^3	7.2315×10^3
$T_i = \eta_i/\mu_i$	N/A	3.9802×10^{-1}	3.3969×10^{-1}	8.3874

Table 3: Identified parameters of free-energy based model

4.3 Model validation

After the model parameters are identified, the generalization ability of the developed model has to be validated. In this section, two groups of experiments are implemented including by setting different driving voltage amplitudes a_i and different voltage frequencies f_i.

4.3.1 Model validation with different driving voltage amplitudes

By setting the amplitudes of the applied voltage as $a_i = 5.5 + 0.5i\ (kV)$ $(i = 1, 2, 3, 4, 5)$ and setting the frequencies of the applied voltage as $f_i = 0.2, 0.4, 0.6, 0.8, 1.0\ (Hz)$, respectively. In this way, the driving voltage has various amplitudes but single frequency in each measured experiment. Figs. 11-13 illustrate the comparison of the model simulation output and measured experimental data under the driving voltage frequencies f_i at $0.2\ (Hz)$, $0.4\ (Hz)$ and $0.8\ (Hz)$, respectively. Moreover, the modeling errors for these various measured experiments are displayed in Table 4.

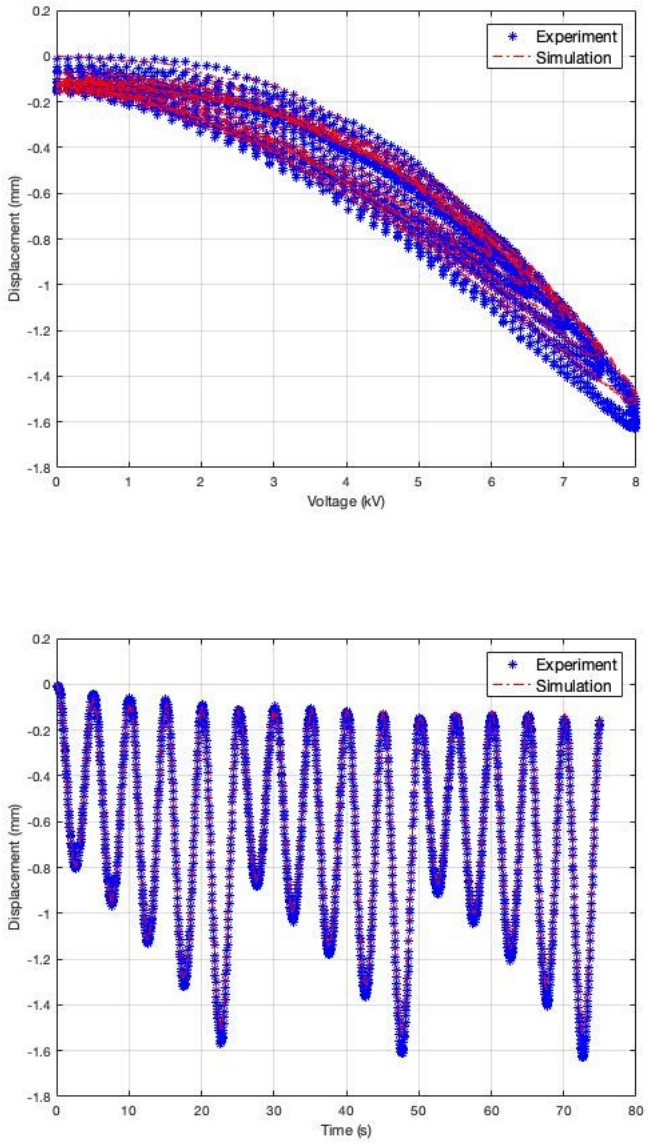

Figure 11: Comparison of model simulation and measured experimental data with driving voltage frequency $f_i = 0.2\ (Hz)$

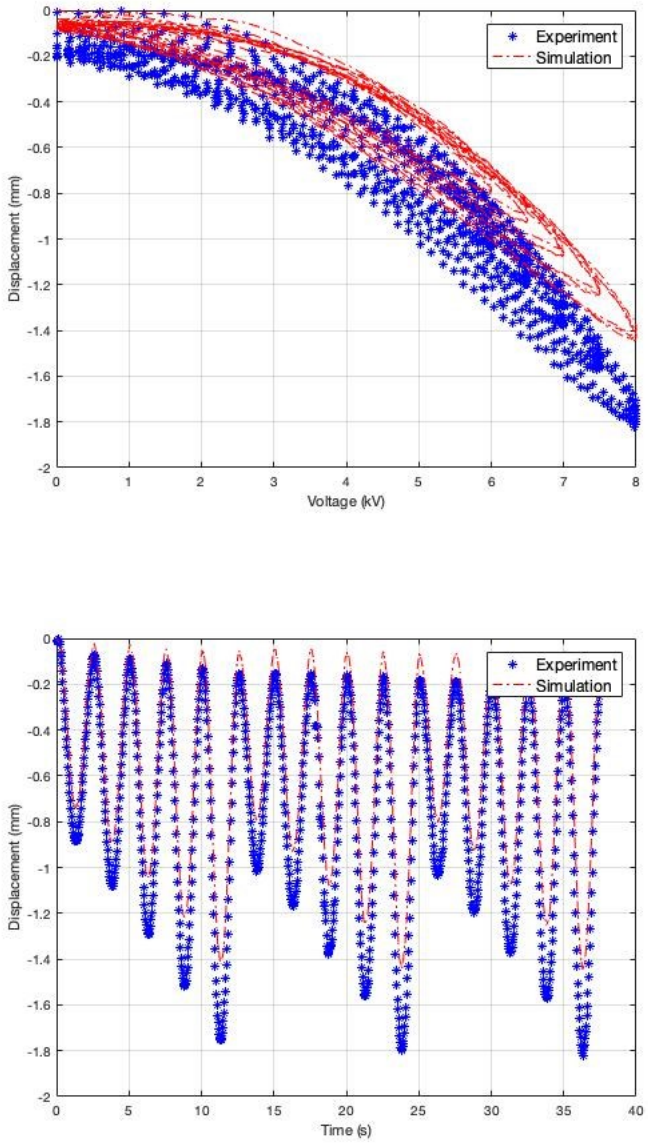

Figure 12: Comparison of model simulation and measured experimental data with driving voltage frequency $f_i = 0.4\ (Hz)$

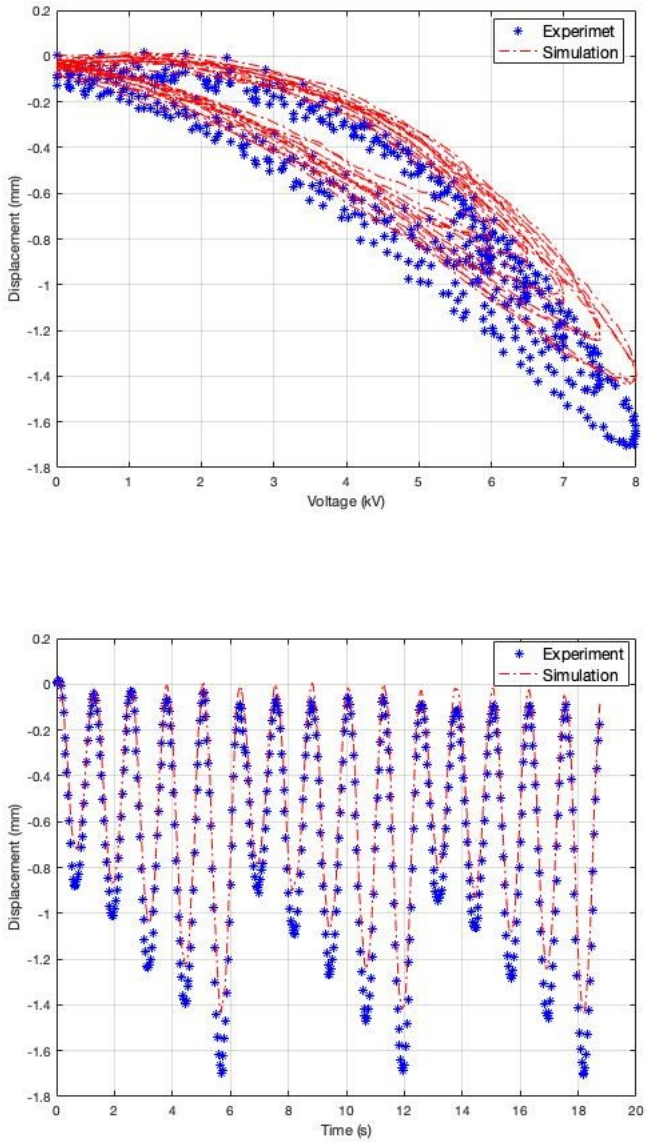

Figure 13: Comparison of model simulation and measured experimental data with driving voltage frequency $f_i = 0.8\ (Hz)$

	e_{rms}	e_m
$f = 0.2(Hz)$	5.8484%	6.9696%
$f = 0.4\ (Hz)$	8.8924%	2.4462%
$f = 0.6\ (Hz)$	5.8952%	3.8678%
$f = 0.8\ (Hz)$	8.7797%	5.8924%
$f = 1.0\ (Hz)$	5.9604%	3.8877%

Table 4: Modeling errors with different driving voltage amplitudes a_i

From the experimental results shown above, the root-mean-square error of the modeling for measured experiments with different driving voltage amplitudes a_i is less than 8.9%. And the maximum modeling error for any collected experimental data is less than 7.0%. When the driving voltage frequency f_i is set at 0.2 (Hz), it's obvious that the maximum modeling error is higher than other conditions. Based on the study of DEA's nonlinearity, it figures out that there is external disturbance for the data collection when at a low driving voltage frequency. Nonetheless, the maximum modeling error tested when $f_i = 0.2\ (Hz)$ is still within the allowable range. Hence, the generalization ability of the developed model of DEA can reach the expectation.

4.3.2 Model validation with different driving voltage frequencies

By setting the amplitudes of the applied voltage as $a_i = 6.0, 6.5, 7.0, 7.5, 8.0\ (kV)$, respectively and setting the frequencies of the applied voltage as $f_i = 0.2i\ (Hz)$. In this way, the driving voltage has various frequencies but single amplitude in each measured experiment.

Figs. 14-16 illustrate the comparison of the model simulation output and measured experimental data under the driving voltage amplitudes a_i at 6.0 (kV), 7.0 (kV) and 8.0 (kV), respectively. Moreover, the modeling errors for these various experiments are displayed in Table 5.

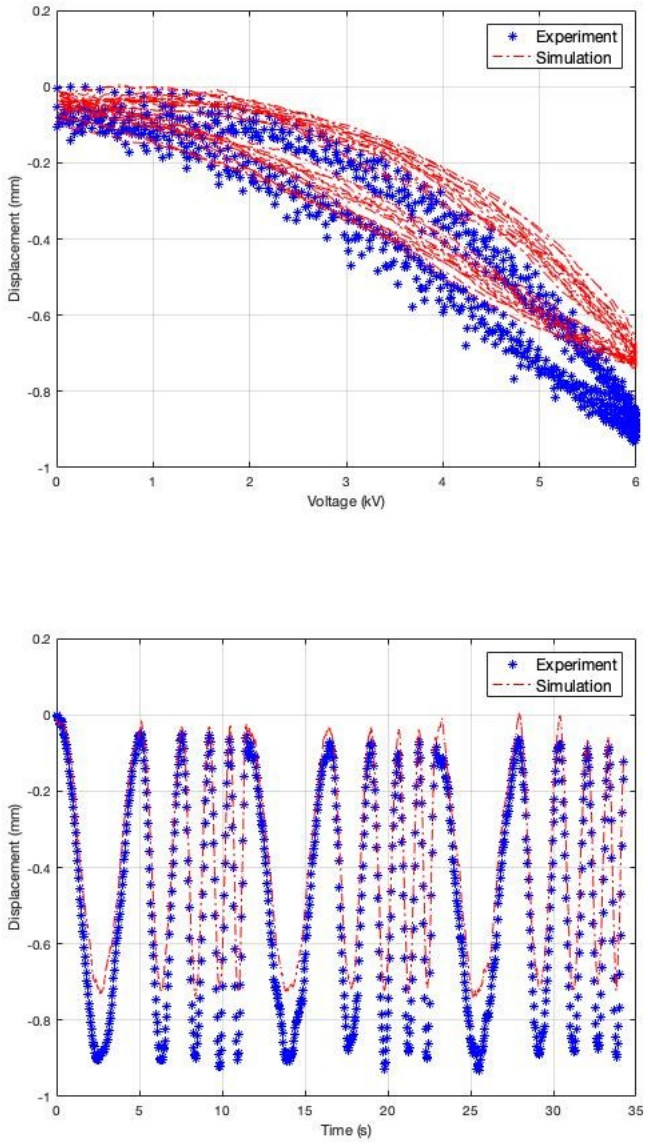

Figure 14: Comparison of model simulation and measured experimental data with driving voltage amplitude $a_i = 6.0\ (kV)$

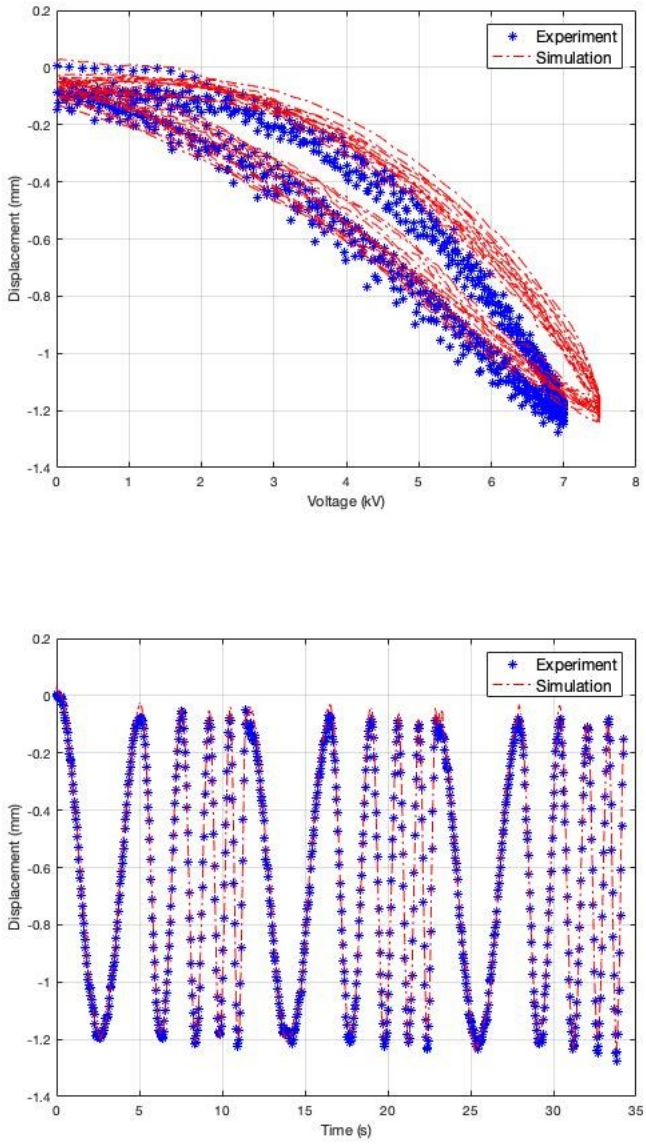

Figure 15: Comparison of model simulation and measured experimental data with driving voltage amplitude $a_i = 7.0\ (kV)$

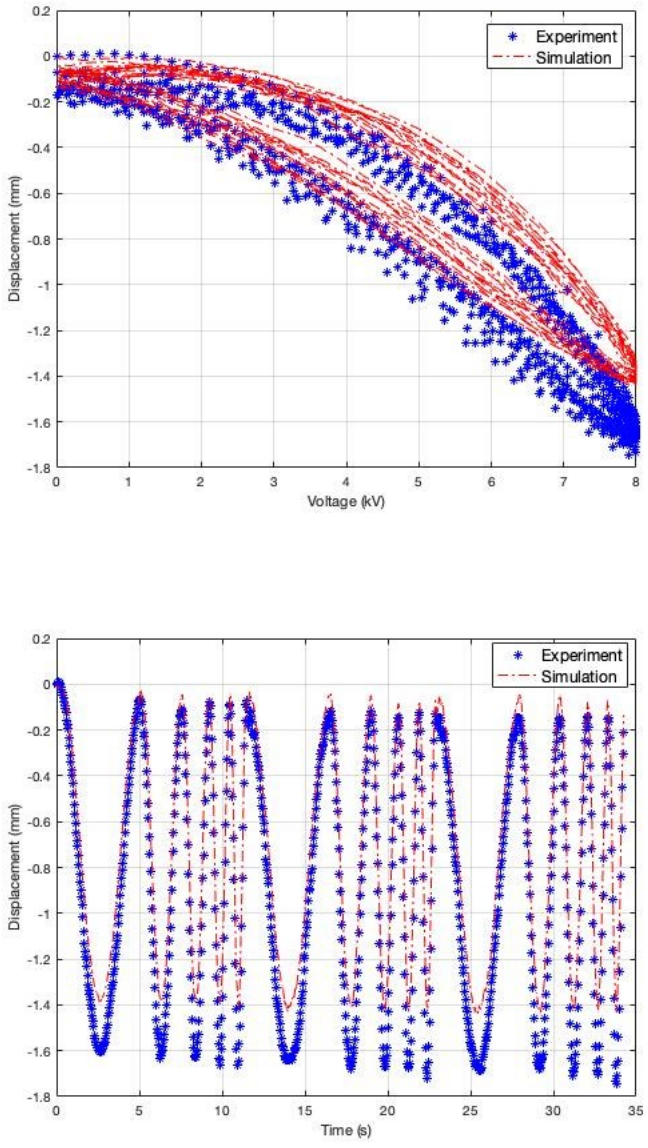

Figure 16: Comparison of model simulation and measured experimental data with driving voltage amplitudes $a_i = 8.0\ (kV)$

	e_{rms}	e_m
$a = 6.0$ (kV)	2.4729%	7.4374%
$a = 6.5$ (kV)	2.9408%	6.7550%
$a = 7.0$ (kV)	3.5766%	7.0148%
$a = 7.5$ (kV)	7.7592%	5.6113%
$a = 8.0$ (kV)	8.6652%	4.6098%

Table 5: Modeling errors with different driving voltage frequencies f_i

From the experimental results shown above, the root-mean-square error of the modeling for measured experiments with different driving voltage frequencies f_i is less than 8.7%. And the maximum modeling error for any collected experimental data is less than 7.5%. According to the results obtained from both groups of test experiments, the generalization of the developed free-energy based model moving in vertical direction can be validated.

4.4 Summary

In this chapter, the meticulous process of setting up experiments to gather accurate data is introduced first, involving the assembly of DEA and instrumentation set up. By employing differential evolution algorithm, the model parameters μ_i, J_i, and T_i are determined. Furthermore, comparing simulation results with experimental data by varying different driving voltage amplitudes and frequencies supports the developed model's accuracy and predictive capability.

Chapter 5

Conclusion and Future Work

5.1 Conclusion

Herein, a free-energy based model to describe the deformation mechanism of dielectric elastomer actuators (DEAs) is proposed with a planar shape moving in vertical direction. First, the schematic and working principle of DEAs is discussed in the introductory sections. Learning from researchers' contributions to modeling mythologies, the Gent model and generalized Maxwell model are selected to present the elastic energy and time-dependent viscoelastic behavior of DEA, respectively. Based on the theory of free energy and thermodynamic nonequilibrium, the relationship between the strain rates and time is found. After that, the parameters of the developed model are empirically identified by implementing differential evolutionary algorithm in MATLAB. Then, by setting different driving voltage amplitudes and frequencies, the comparisons of model simulation and experimental results are obtained. Hence, the generalization of the proposed model is demonstrated which is also able to explain the intricate nonlinear characteristics and complex electromechanical coupling of DEAs.

5.1 Future work

The deformation of dielectric elastomer actuators (DEAs) is not only subject to various driving voltage amplitudes and frequencies, but also subject to the temperature and humidity of the working environment. In the future work, more experiments are planned to be implemented to investigate how DEAs perform when at different patterns of temperature and humidity. Also, from the experimental results, further studies can be pursed including developing a more precise model with higher accuracy by taking into consideration nonlinearities other than creep and hysteresis. Besides, inspired by the worm-like soft robot which could inspect, and repair on-wing aircraft engines built by GE Aerospace, USA, we will develop suitable controllers combining with the dynamic model to investigate the applications in aerospace industry.

References

[1] Y. Qiu, E. Zhang, R. Plamthottam, and Q. Pei. Dielectric elastomer artificial muscle: materials innovations and device explorations. *Accounts of Chemical Research*, 52(2): 316-325, 2019.

[2] N.C. Goulbourne, E.M. Mockensturm, and M.I. Frecker. Electro-elastomers: large deformation analysis of silicone membranes. *International Journal of Solids and Structures*, 44(9): 2609-2626, 2007.

[3] Y. Yang, C. Ai, W. Chen, J. Zhen, X. Kong, and Y. Jiang. Recent advances in sources of bio- inspiration and materials for robotics and actuators. *Small Methods*, 7(9): 2300338, 2023.

[4] N. Mathews. Novel material composites for dielectric elastomer actuators. 2019.

[5] M.H. Rahman, H. Wert, A. Goldman, Y. Hida, C. Diesner, L. Lane, and P.L. Menezes. Recent progress on electroactive polymers: synthesis, properties and applications. *Ceramics*, 4(3): 516-541, 2021.

[6] M. Alkhathami. Modeling of a dielectric elastomer (Doctoral dissertation, *Concordia University*). 2018.

[7] K., Naito, Y. Miwa, R. Ando, K. Yashiro, and S. Kutsumizu. Evaluation for the actuation performance of dielectric elastomer actuator using polyisoprene elastomer with dynamic ionic crosslinks. *Sensors and Actuators A: Physical*, 332: 113143, 2021.

[8] Z. Shen, F. Chen, X. Zhu, K.T. Yong, and G. Gu. Stimuli-responsive functional materials for soft robotics. *Journal of Materials Chemistry B*, 8(39): 8972-8991, 2020.

[9] L.J. Romasanta, M.A. López-Manchado, and R. Verdejo. Increasing the performance of dielectric elastomer actuators: A review from the materials perspective. *Progress in Polymer Science*, 51: 188-211, 2015.

[10] P. Ariano, D. Accardo, M. Lombardi, S. Bocchini, L. Draghi, L. De Nardo, and P. Fino. Polymeric materials as artificial muscles: an overview. *Journal of Applied Biomaterials & Functional Materials*, 13(1): 1-9, 2015.

[11] S.W. Park, S.J. Kim, S.H. Park, J. Lee, H. Kim, and M.K. Kim. Recent progress in development and applications of ionic polymer–metal composite. *Micromachines*, 13(8): 1290, 2022.

[12] M. Shahinpoor. Fundamentals of ionic polymer metal composites (IPMCs). *Ionic Polymer Metal Composites (IPMCs): Smart Multi-Functional Materials and Artificial Muscles*, 1: 1-60, 2015.

[13] Z. Zhu, C. Bian, J. Ru, W. Bai, and H. Chen. Rapid deformation of IPMC under a high electrical pulse stimulus inspired by action potential. *Smart Materials and Structures*, 28(1): 01LT01, 2018.

[14] M. Li, A. Pal, A. Aghakhani, A. Pena-Francesch, and M. Sitti. Soft actuators for real-world applications. *Nature Reviews Materials*, 7(3): 235-249, 2022.

[15] W. Zeng, L. Shu, Q. Li, S. Chen, F. Wang, and X.M. Tao. Fiber- based wearable electronics: a review of materials, fabrication, devices, and applications. *Advanced Materials*, 26(31): 5310-5336, 2014.

[16] J.S. Plante, and S. Dubowsky. Large-scale failure modes of dielectric elastomer actuators. *International journal of solids and structure*s, 43(25-26): 7727-7751, 2006.

[17] Y. Guo, L. Liu, Y. Liu, and J. Leng. Review of dielectric elastomer actuators and their applications in soft robots. *Advanced Intelligent Systems*, 3(10): 2000282, 2021.

[18] D.P. Muffoletto, K.M. Burke, and J.L. Zirnheld. Partial discharge analysis of prestretched and unstretched acrylic elastomers for dielectric elastomer actuators (DEA). *Electroactive Polymer Actuators and Devices (EAPAD)*, 8340: 494-501, 2012.

[19] L. Liu, Y. Huang, Y. Zhang, E. Allahyarov, Z. Zhang, F. Lv, and L. Zhu. Understanding reversible Maxwellian electroactuation in a 3M VHB dielectric elastomer with prestrain. *Polymer*, 144: 150-158, 2018.

[20] C. Jordi, A. Schmidt, G. Kovacs, S. Michel, and P. Ermanni. Performance evaluation of cutting-edge dielectric elastomers for large-scale actuator applications. *Smart Materials and Structures*, 20(7): 075003, 2011.

[21] F. Carpi, P. Chiarelli, A. Mazzoldi, and D. De Rossi. Electromechanical characterisation of dielectric elastomer planar actuators: comparative evaluation of different electrode materials and different counterloads. *Sensors and Actuators A: Physical*, 107(1): 85-95, 2002.

[22] W. Zang, X. Liu, J. Li, Y. Jiang, B. Yu, H. Zou, N. Ning, M. Tian, and L. Zhang. Conductive, self-healing and recyclable electrodes for dielectric elastomer generator with high energy density. *Chemical Engineering Journal*, 429: 132258, 2022.

[23] R. Shankar, T.K. Ghosh, and R.J. Spontak. Dielectric elastomers as next-generation polymeric actuators. *Soft Matter*, 3(9): 1116-1129, 2007.

[24] M. Lallart, P.J. Cottinet, D. Guyomar, and L. Lebrun. Electrostrictive polymers for mechanical energy harvesting. *Journal of Polymer Science Part B: Polymer Physics*, 50(8): 523-535, 2012.

[25] P. Segura, O. Lobato-Calleros, A. Ramírez-Serrano, and I. Soria. Human-robot collaborative systems: Structural components for current manufacturing applications. *Advances in Industrial and Manufacturing Engineering*, 3: 100060, 2021.

[26] R. Bogue. Underwater robots: a review of technologies and applications. *Industrial Robot: An International Journal*, 42(3):186-191, 2015.

[27] W. Cui, L. Lian, and G. Pan. Frontiers in deep-sea equipment and technology. *Journal of Marine Science and Engineering*, 11(4): 715, 2023.

[28] G. Li, X. Chen, F. Zhou, Y. Liang, Y. Xiao, X. Cao, Z. Zhang, M. Zhang, B. Wu, S. Yin, and Y. Xu. Self-powered soft robot in the Mariana Trench. *Nature*, 591(7848): 66-71, 2021.

[29] H. Godaba, J. Li, Y. Wang, and J. Zhu. A soft jellyfish robot driven by a dielectric elastomer actuator. *IEEE Robotics and Automation Letters*, 1(2): 624-631, 2016.

[30] G. Li, T.W. Wong, B. Shih, C. Guo, L. Wang, J. Liu, T. Wang, X. Liu, J. Yan, B. Wu, and F. Yu. Bioinspired soft robots for deep-sea exploration. *Nature Communications*, 14(1): 7097, 2023.

[31] G. Fang, and J. Cheng. Advances in climbing robots for vertical structures in the past decade: A Review. *Biomimetics*, 8(1): 47, 2023.

[32] G. Gu, J. Zou, R. Zhao, X. Zhao, and X. Zhu. Soft wall-climbing robots. *Science Robotics*, 3(25): eaat2874, 2018.

[33] L. Chen, M. Ghilardi, J.J. Busfield, and F. Carpi. Electrically tunable lenses: a review. *Frontiers in Robotics and AI*, 8: 678046, 2021.

[34] F. Hartmann, L. Penkner, D. Danninger, N. Arnold, and M. Kaltenbrunner. Soft tunable lenses based on zipping electroactive polymer actuators. *Advanced Science*, 8(3): 2003104, 2021.

[35] S. Nam, S. Yun, J.W. Yoon, S.K. Park, S. Mun, B. Park, and K.U. Kyung. A robust soft lens for tunable camera application using dielectric elastomer actuators. *Soft Robotics*, 5(6): 777-782, 2018.

[36] C. Cao and A.T. Conn. Performance optimization of a conical dielectric elastomer actuator. *Actuators*, 7(2): 32, 2018.

[37] C. Cao, S. Burgess, and A.T. Conn. Toward a dielectric elastomer resonator driven flapping wing micro air vehicle. *Frontiers in Robotics and AI*, 5: 137, 2019.

[38] J. Zou and G. Gu. Dynamic modeling of dielectric elastomer actuators with a minimum energy structure. *Smart Materials and Structures*, 28(8): 085039, 2019.

[39] P. Huang, W. Ye, and Y. Wang. Dynamic modeling of dielectric elastomer actuator with conical shape. *Plos one*, 15(8): e0235229, 2020.

[40] L. Liu, H. Chen, J. Sheng, J. Zhang, Y. Wang, and S. Jia. Experimental study on the dynamic response of in-plane deformation of dielectric elastomer under alternating electric load. *Smart Materials and Structures*, 23(2): 025037, 2014.

[41] R.E. Pelrine, R.D. Kornbluh, and J.P. Joseph. Electrostriction of polymer dielectrics with compliant electrodes as a means of actuation. *Sensors and Actuators A: Physical*, 64(1): 77-85, 1998.

[42] M. Wissler and E. Mazza. Electromechanical coupling in dielectric elastomer actuators. *Sensors and Actuators A: Physical*, 138(2): 384-393, 2007.

[43] Z. Suo. Theory of dielectric elastomers. *Acta Mechanica Solida Sinica*, 23(6): 549-578, 2010.

[44] G.Y. Gu, U. Gupta, J. Zhu, L.M. Zhu, and X. Zhu. Modeling of viscoelastic electromechanical behavior in a soft dielectric elastomer actuator. *IEEE Transactions on Robotics*, 33(5): 1263-1271, 2017.

[45] B. Kim, S.B. Lee, J. Lee, S. Cho, H. Park, S. Yeom, and S.H. Park. A comparison among Neo-Hookean model, Mooney-Rivlin model, and Ogden model for chloroprene rubber. *International Journal of Precision Engineering and Manufacturing*, 13: 759-764, 2012.

[46] S.K. Melly, L. Liu, Y. Liu, and J. Leng. A review on material models for isotropic hyperelasticity. *International Journal of Mechanical System Dynamics*, 1(1): 71-88, 2021.

[47] J. Wang, Q. Wang, and H.H. Dai. Stress-free bending of a Neo-Hookean plate induced by growth: Exact solution and experiments. *International Journal of Non-Linear Mechanics*, 106: 280-287, 2018.

[48] M. Hossain and P. Steinmann. Modelling and simulation of the curing process of polymers by a modified formulation of the Arruda–Boyce model. *Archives of Mechanics*, 63(5-6): 621-633, 2011.

[49] A.N. Gent. A new constitutive relation for rubber. *Rubber Chemistry and Technology*, 69(1): 59-61, 1996.

[50] E. Pucci and G. Saccomandi. A note on the Gent model for rubber-like materials. *Rubber Chemistry and Technology*, 75(5): 839-852, 2002.

[51] L. Dunn. Introduction to viscoelasticity in polymers and its impact on rolling resistance in pneumatic tyres. *International Journal of Squiggly and Wobbly Materials*, 23, 2019.

[52] A. Morro. Modelling of viscoelastic materials and creep behaviour. *Meccanica*, 52(13): 3015-3021, 2017.

[53] T. Nguyen, J. Li, L. Sun, D. Tran, and F. Xuan. Viscoelasticity modeling of dielectric elastomers by Kelvin Voigt-generalized Maxwell model. *Polymers*, 13(13): 2203, 2021.

[54] R. Greco and G.C. Marano. Identification of parameters of Maxwell and Kelvin-Voigt generalized models for fluid viscous dampers. *Journal of Vibration and Control*, 21(2): 260-274, 2015.

[55] R. Storn and K. Price. Differential evolution–a simple and efficient heuristic for global optimization over continuous spaces. *Journal of Global Optimization*, 11: 341-359, 1997.

[56] N. Nouhi. Modeling of dielectric elastomer actuators with a conical shape (Doctoral dissertation, *Concordia University*), 2021.